Enhancing the Resolution of Inkjet Printing Through Modification of Ink/Substrate Interaction

by

Maryam Masroor Shalmani

Advisor

Professor Pratap M. Rao

A Dissertation
Submitted to the Faculty
of the
WORCESTER POLYTECHINC INSTITUTE
in partial fulfillment of the requirements for the
Degree of Doctor of Philosophy
in
Mechanical Engineering
June, 2022

Abstract

The focus of this research is on optimizing the performance of inkjet printing using the Meyer Burger PiXDRO LP50 printing platform and KM512-SH printhead with commercially available ink and substrates, focusing on print resolution to overcome one of the two main barriers that are currently preventing inkjet printing from being adopted for prototyping and volume manufacturing which are print reliability and print resolution. We would pursue three approaches to enhance inkjet printing resolution. In the first approach, we will study the properties of selected ink and substrates to understand their separate and combined influence on print resolution and we will try to find an optimized print setting based on the knowledge we gained from it. In the second and third approaches, we will physically and chemically modify the selected substrates using nanoimprint lithography (NIL), and Layer-by-layer Self-assembly (LbL) methods and we will study the effect of these surface modifications methods on print resolution.

ACKNOWLEDGEMENTS

I want to deeply acknowledge my advisor, Professor Pratap M. Rao, for providing me the opportunity to work on this project and his constant guidance and encouragement during my Ph.D. study.

I also want to express my sincere gratitude to Professor Danielle Cote, Professor Yihao Zheng, Professor Liu Yuxiang, Professor Aswin Gnanaskandan, and Professor Kyle Tsaknopoulos for their help, encouragement and serving in my thesis committee.

Meanwhile, I want to thank all my friends in Nanoenergy Lab, my colleague Nick Pratt for sharing part of the results of his research with me which is included in Chapter 3 of my thesis, as well as all the staff and faculty in Mechanical Engineering Department for their help.

Finally, I would like to thank my family for their constant support and encouragement.

Table of Contents

CHAPTER 1 5

INTRODUCTION 5

1.1. FLEXIBLE HYBRID ELECTRONICS 6
1.2. PRINTING TECHNOLOGIES 6
1.3. INK-SUBSTRATE INTERACTION 8

CHAPTER 2 9

OBJECTIVES AND SCOPE 9

CHAPTER 3 12

ENHANCING THE INKJET RESOLUTION THROUGH CHARACTERIZATION OF INK, SUBSTRATES AND THEIR INTERACTION 12

3.1. INTRODUCTION 13
3.2. OBJECTIVES AND SCOPE 17
3.3. APPROACH AND METHODS 18
3.4. RESULTS AND DISCUSSION 20
  3.4.1. Surface Tension Measurements of Ink *20*
  3.4.2. Viscosity Measurement of Ink *21*
  3.4.3. Contact Angle of Ink on Substrate *22*
  3.4.4. Printability of Ink *24*
  3.4.5. Jetting Parameters *26*
  3.4.5. Effect of drop spacing and contact angle on print resolution *27*
  3.4.6. Effect of substrate temperature on print resolution *29*

CHAPTER 4 32

NANOIMPRINT LITHOGRAPHY (NIL) PATTERNED SURFACES FOR HIGH-RESOLUTION INKJET PRINTING 32

4.1. INTRODUCTION 33
4.2. OBJECTIVES AND SCOPE 35
4.3. APPROACH AND METHODS 35
4.4. RESULTS AND DISCUSSION 37
  4.4.1. Contact Angle of Ink *37*
  4.4.2. Printed Traces on Microfeatures *37*
4.5. CONCLUSIONS 43

CHAPTER 5 45

NANOIMPRINT LITHOGRAPHY (NIL) MICROCHANNELS FOR HIGH RESOLUTION INKJET PRINTING 45

5.1. INTRODUCTION 46
5.2. OBJECTIVES AND SCOPE 47
5.3. APPROACH AND METHODS 47
  Keyence VHX-7000 microscope was used for imaging, and KLA Tencor AlphaStep D-600 Stylus Profilometer was used for profile measurement of the printed traces inside the microchannels. *48*
5.4. RESULTS AND DISCUSSION 48
  5.4.1. Preliminary Results *48*

5.5. Conclusions 54

CHAPTER 6 .... **55**

INVESTIGATION OF THE EFFECT OF SURFACE FUNCTIONALIZATION WITH LAYER-BY-LAYER SELF-ASSEMBLY ON THE INTERACTION OF INK AND SUBSTRATES **55**

6.1. Introduction 56
6.2. Objectives and Scope 57
6.3. Approach and Methods 57
6.4. Results and Discussion 58
  6.4.1. Contact Angle of Ink *58*
  6.4.2. Prints on Kapton FN and LBL coated Kapton FN *59*
  6.4.3. Adhesion of Dupont PE410 to Kapton FN and LbL coated Kapton FN *63*
6.5. Conclusions 63

CHAPTER 7 .... **64**

CONCLUSIONS AND FUTURE WORK **64**

CHAPTER 8 .... **67**

OTHER RESEARCH PROJECTS, PUBLICATIONS TO DATE AND PLANNED PUBLICATIONS **67**

8.1. Controlling crystal growth of non-toxic Bismuth iodide (BiI3) semiconducting material for efficient photovoltaics 68
  8.1.1. Introduction *68*
  8.1.2. Approach and Methods *70*
  8.1.3. Results and Discussion *71*
  8.1.4. Conclusions *77*
8.2. Publications To Date 78
8.3. Planned Publications 78

REFERENCES **79**

Chapter 1

Introduction

1.1. Flexible Hybrid Electronics

Over the last few years, forms of electronics have started to change from traditional rigid ones to nontraditional electronics that are flexible and stretchable[1]. Despite recent advances in the developments of flexible and stretchable electronics, they still have a few limitations compared to silicon integrated circuits (ICs) such as low performance, high power consumption and limited lifetime. On the other hand, silicon ICs are bulky, and their manufacturing is expensive, and it is hard to manufacture them in large-area scales. Flexible hybrid electronics (FHEs), which are a combination of silicon ICs and flexible and stretchable electronics, enable us to take advantage of flexibility, cost-effectiveness, and large-scale manufacturability of flexible electronics along with low power and high-performance computing capability of silicon ICs[2], [3]. An example of a FHE system is shown in Figure 1.

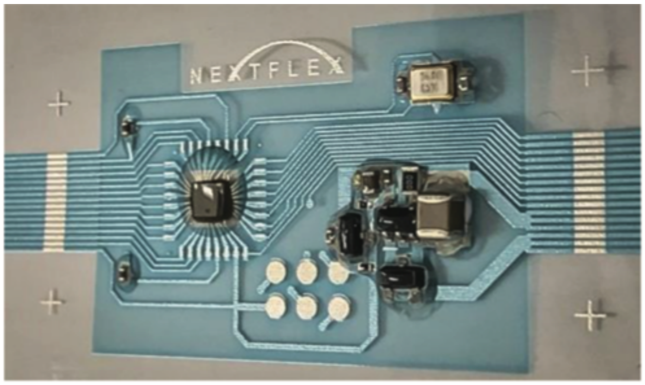

Figure 1. An example of a FHE: A printed and flexible Arduino made by NextFlex [4].

1.2. Printing Technologies

Printing is an applicable manufacturing technology for the fabrication of FHEs. FHE devices require high-resolution, high-throughput, and reliable printing methods for prototyping and volume manufacturing. Screen printing is the most commonly used and mature process for fabrication of FHEs, both for prototyping and volume manufacturing. The limitations for this process are that a patterned screen must be created first, which adds expense and time, that the screen is difficult to clean, that the minimum feature size/spacing is relatively large (~100 μm), that there is large wastage of ink, and that the deposited film is rough because inks that are highly viscous (500-5000 cp) are used in this printing method[3], [5] Gravure printing is a roll-to-roll printing technique that is attractive for volume manufacturing of FHEs and feature size/spacing of down to ~10 μm can be achieved by using this printing method. The limitations are that it requires the fabrication of an expensive pattern (master roll) and demanding optimization to achieve high resolution printing[6]. Aerosol jet is a digital manufacturing tool that achieves feature size down to ~10 μm. The limitations are overspray and resulting poor edge definition, relatively low throughput, and high expense[5], [7].

Inkjet printing is a digital printing process that enables printing directly from digital design files, allows for rapid error correction and design changes, and can have low operation costs (for an optimized process). In addition, drop-on-demand inkjet printheads with hundreds of nozzles and drop ejection from each nozzle at kHz frequencies can enable relatively high throughput, making inkjet suitable for not only prototyping, but also volume manufacturing. Inkjet features accurate positioning of precise picolitre-volume drops, which can enable conductive traces with widths theoretically as small as the droplet size (e.g. 24 μm droplet diameter for 4 picolitre volume drops). Additionally, inkjet is non-contact and supports a range of conductive, dielectric, and other functional inks[3], [5]. A comparison of FHE manufacturing techniques is shown in Table 1.

Printed FHEs have wide range of applications. They have mostly been used in healthcare realm. Their flexibility and the fact that they can be wrapped around parts of human body make them a good candidate for sensing medical devices that can monitor vital signs such as pulse oxygenation, temperature, heart rate, respiration rate, and blood pressure[8]. In the past few years, the application of printed FHEs expanded from medical devices to industrial, environmental, and agricultural multisensor devices that monitor humidity, gas, and goods [9], [10]

Table 1. Comparison of FHE manufacturing technologies**.**

Process	**Type**	**Min. Feature Size/Spacing**	**Throughput (m^2/sec)**	**Cost**
Screen	Pattern-based	~100 μm	~10	Medium (small volume) Low (large volume)
Gravure		~10 μm	~10	High (small volume); Low (large volume)

Aerosol Jet	Digital	~10 µm	$\sim 10^{-5*}$	High
Inkjet		~100 µm achieved Our goal<100 µm	~10 Possible	Low (for optimized process)

*Continuous production of 30,000 units of 300 mm^2 antenna arrays per week [11].

1.3. Ink-Substrate Interaction

Inkjet printing can open up new FHE manufacturing opportunities, but for it to be an attractive process for prototyping and volume manufacturing of FHEs, it should achieve acceptable resolution (our goal is < 100 µm). The most important factor to focus on for enhancing print resolution is having a precise understanding of fluid dynamic properties of the inks and the ink/substrate interaction after droplet injection from the printhead and after droplet impact on the substrate. We will pursue this goal through studying the properties of the selected ink and substrates, and physically and chemically modifying the substrates.

Chapter 2

Objectives and Scope

Our objective is to focus on optimizing the performance of inkjet printing using the Meyer Burger PiXDRO LP50 printing platform and KM512-SH printhead with commercially available ink and substrates, focusing on print resolution to overcome one of the two main barriers that are currently preventing inkjet printing from being adopted for prototyping and volume manufacturing. The KM512-SH is a piezoelectric drop-on-demand printhead that has 512 nozzles and ~4pL drop volume. Figure 2 shows a picture of a Meyer Burger PiXDRO LP50 printer.

Figure 2. Meyer Burger PiXDRO LP50 printing.

To enhance print resolution, we plan to investigate three main approaches:

1. In the first approach, we will study the properties of selected ink and substrates to understand their separate and combined influence on print resolution. We will try to find an optimized print setting based on the knowledge we gained from studying ink/substrate properties and their interaction for enhancing print resolution.

2. In the second approach, we will physically modify the surface of selected substrates by patterning them with microfeatures and microchannels using nanoimprint lithography and studying the effect of the modification on print resolution.

3. In the last approach, we will chemically modify the surface of a selected substrate using Layer-by-layer Self-assembly and study the effect of this chemical modification on print resolution.

Chapter 3

Enhancing the Inkjet Resolution Through Characterization of Ink, Substrates and Their Interaction

3.1. Introduction

To be able to jet a fluid ink successfully and to subsequently have an acceptable print resolution, we need to have a precise understanding of fluid dynamic properties of the inks and the ink/substrate interaction after droplet injection from the printhead and after droplet impact on the substrate [12].

As mentioned in chapter 2, we use a printhead with piezoelectric drop-on-demand nozzles for jetting the drops. Several dimensionless physical constants, which are derived from rheological parameters of the ink, can be used to characterize the behavior of liquid droplets among which, Reynolds (*Re*), Weber (*We*), and Ohnesorge (*Oh*) numbers are the most useful ones that are formulated as follows:

$$Re=\frac{\mathrm{v}\rho a}{\eta} \qquad (1)$$

$$We = \frac{v^2\,\rho a}{\gamma} \qquad (2)$$

$$Oh = \frac{\sqrt{We}}{Re} = \frac{\eta}{\sqrt{\gamma\rho a}} \qquad (3)$$

Here, ρ, η, and γ are the density, dynamic viscosity, and surface tension of the fluid respectively, v is the velocity, and a is a characteristic length, and fluid is assumed to have linear Newtonian behavior.

Fromm [13] introduced Ohnesorge (*Oh*) number and another form of it, $z = \frac{1}{Oh}$, as a physical number that is a combination of Reynold (*Re*) and Weber (*We*) number, which is a criterion for drop formation. Using numerical simulation, a range for stable drop formation based on Z was introduced. For $Z < 1$, viscous dissipation prevents drop ejection from printhead, and for $Z > 10$, a secondary drop named satellite drop will accompany the primary ejected droplet, which will affect print resolution, so the range of Z for stable drop formation would be $1 < Z < 10$ [14]. Besides Z, the fluid/air surface tension at the nozzle can act as a barrier against drop ejection from the nozzle. To overcome this barrier, the droplet should possess a minimum velocity, v_{min}, that is formulated in terms of Weber number [15]:

$$We = v_{min} \left(\frac{\rho d_n}{\lambda}\right)^{0.5} > 4 \qquad (4)$$

In this formula, d_n is nozzle diameter.

As mentioned above, the ink/substrate interaction when the ejected droplet impacts the substrates also needs to be considered and this interaction is one of the factors that defines the print resolution. A grouping of dimensionless numbers are stablished for determining the onset of splashing [16]:

$$We^{0.5} Re^{0.25} > f(R) \qquad (5)$$

Here f (R) is only a function of surface roughness and for a smooth and flat surface it is ~50(20).

Using equations 4, 5, and the acceptable range for Z, a map, shown in Figure 3, with relates *Re* and *We* can be sketched, showing different regions and the acceptable range for drop formation [17]. These ranges were validated using a large range of particle-filled fluids [18].

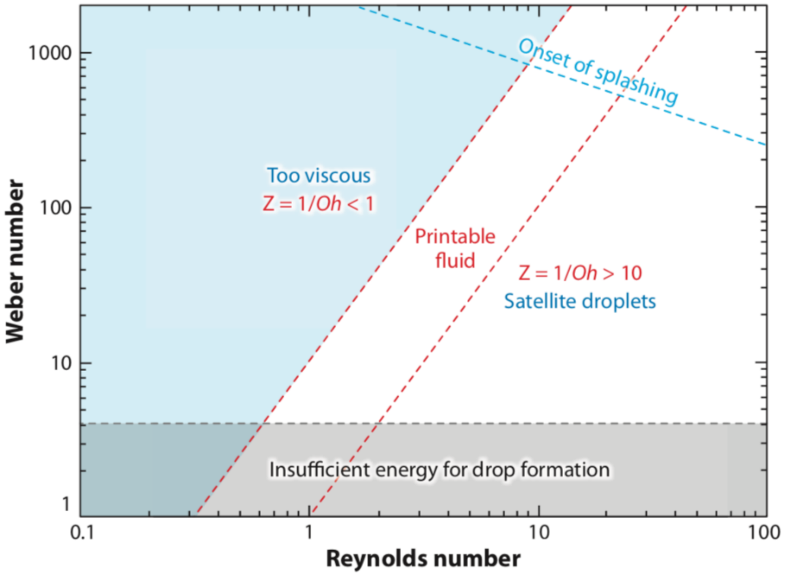

Figure 3. Map of acceptable range for drop formation [17].

The drop would undergo two steps after its impact on the substrate. First, it will spread to a diameter, d_{con}, which is the contact diameter or wetted drop diameter. This diameter depends on the volume of the drop after it is jetted from the nozzle and the equilibrium contact angle, θ. d_o is the diameter of ejected drop in this formula. As seen in formula 6, the equilibrium contact angle plays an essential role in controlling the feature size, resolution, of the printed patterns [17].

$$d_{con} = d_o \sqrt[3]{\frac{8}{\tan\frac{\theta}{2}\ (3 + tan^2\ \frac{\theta}{2})}} \qquad (6)$$

Assuming the printed drop dries with pinned contact lines, the final dried drop diameter will equal the initial wetted diameter. The wetted diameter decreases as the ink-substrate contact angle increases for a drop of fixed volume leading to the potential for higher resolution printing. Figure 4 shows the relationship between contact angle and wetted drop diameter.

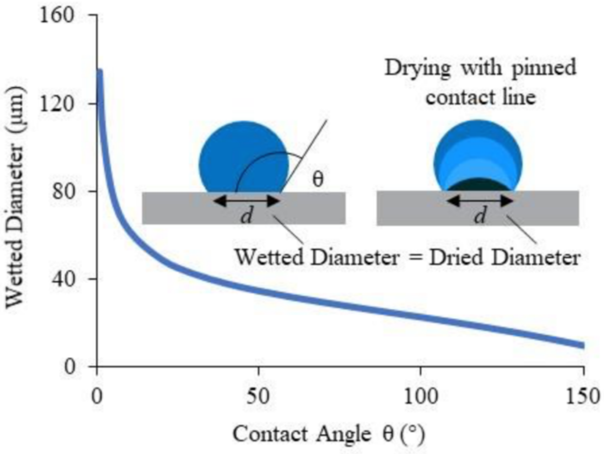

Figure 4. Influence of contact angle on wetted drop diameter.

The second step that a drop will undergo after hitting the substrates is its interaction with its adjacent drops. To have a continuous printed line, the drops need to coalesce and form a bead, and after overlap of adjacent beads a coalesced line can form; however, three types of behavior can occur, which affects the formation and resolution of printed lines.

The first behavior that can happen, which is explained by Duineveld [19], is bulging instability. Bulging happens when the capillary spreading of a drop is slow, and the drop spacing is too small. In this case, the newly deposited drop flows back into the preexisting bead due to the difference in Laplace pressure of the newly printed drop and the leading edge of the preexisting bead. This will cause the preexisting bead to expand and results in a bulging instability. Figure 5 shows a schematic of a bulge instability.

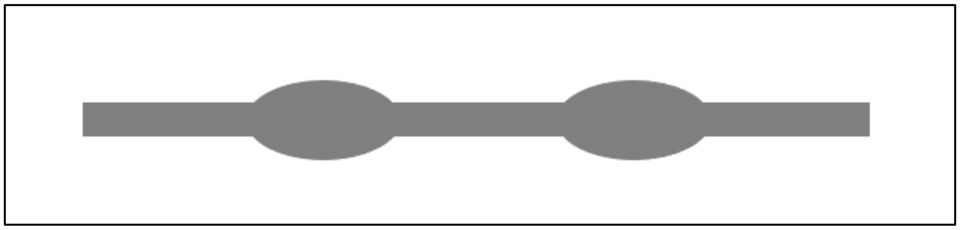

Figure 5. Schematic of a bulged line.

When the drop spacing is slightly smaller than the wetted drop diameter (diameter after hitting the substrate, not d_o), the drops coalesce but they would still maintain their individual rounded contact line, this behavior is called scalloping. The width of scalloped lines is narrower than the diameter of an individual drop since the drops partially coalesced and could not expand [20]. Figure 6 shows a schematic of a scalloped line.

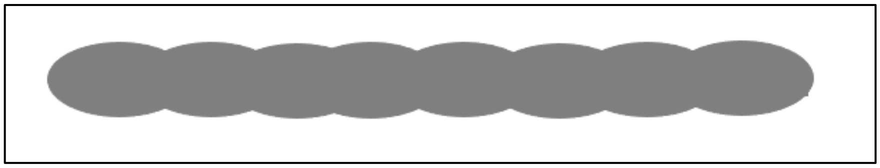

Figure 6. Schematic of a scalloped line.

When the substrate temperature is high enough that the drop drying time is less than drop jetting period, each individual drop will fully dry before the next drop is placed and regardless of the overlap, the line would be like a stack of coins printed on top of each other, as shown in Figure 7 [20]. This type of behavior would result in a rough surface and the chance of ink hitting the rough surface and splashing to the sides, spill over, increases.

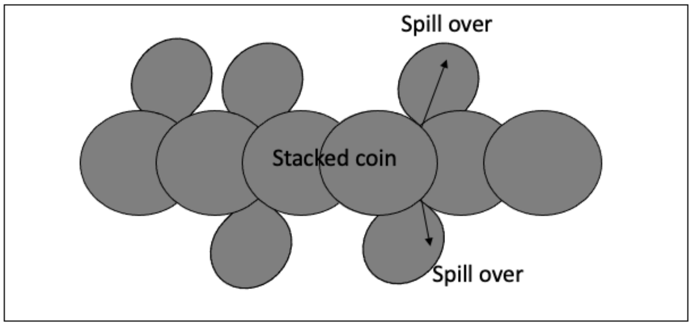

Figure 7. Schematic of stacked coin line.

The above-mentioned points highlight the importance of having an in-depth understanding of the fluid dynamic properties of inks, and optimization of ink/substrate interaction to maximize print resolution.

3.2. Objectives and Scope

As mentioned in Chapter 2, one of the three approaches that we will investigate to enhance print resolution is the selection of suitable printing parameters through a thorough understanding of the properties of the inks, the substrates, and their interaction. In this chapter, our objectives to fulfill this goal are as follows:

1. Study the fluid dynamic properties of the selected ink using surface tension and viscosity measurements and apply these properties to determine dimensionless numbers that enable an understanding of the inkjet drop formation process.
2. Study the ink/substrate interaction using contact angle of ink on selected substrates and apply this knowledge to understand the width and structure of printed lines as a function of drop spacing.
3. Study the role of substrate temperature on print resolution

3.3. Approach and Methods

Three types of inks are used for printing an electronic device: metallic, insulating, and semiconducting inks. Metallic inks are used for connecting multiple electronic elements as interconnects, and for contacts. Silver, gold, and copper nanoparticle suspensions are common metallic inks that are used for this purpose[3]. Silver nanoparticles have high electrical conductivity like gold and copper nanoparticles; however, silver has lower cost relative to gold, and forms a conductive oxide whereas copper forms an insulating oxide. That is why silver nanoparticles are widely used in various applications that use inkjet printing. In this study, we would be evaluating Dupont PE410 silver conductive ink (Solvent-based, 45% Ag loading, 20-40 cP @ 25°C) as our conductive ink because of its high loading of silver nanoparticles and its compatibility with KM512-SH printhead.

The following commercial off the shelf substrates will be evaluated in this project:

- PET ST-505 (with solvent adhesion coating)
- Dupont Kapton 500FN131
- Fluorinated ethylene propylene (FEP)

Polyethylene terephthalate (PET) ST-505 is chosen because it is economical and commonly used for printing electronics. The solvent adhesion coating results in a relatively small contact angle but it provides good adhesion of the printed materials to the substrate. Kapton (polyimide) is chosen because it is commonly used for printing electronics that will need to survive higher temperatures. However, its disadvantage is that ink spreads out on the substrate due to low contact angle, leading to lower printing resolution. Kapton 500FN131 is polyimide having a fluoropolymer coating, which can provide a large ink/substrate contact angle leading to potential for better print resolution. FEP (fluorinated ethylene propylene) is another substrate, that also has large ink contact angle.

Surface tensions of the ink were measured using the Goniometer/tensiometer (Rame-Hart Model 210), by the pendant drop method at room temperature. The ink was prepared according to the manufacturer's recommendation (i.e. shaking or bottle rolling, filtering, etc.). Surface tension was measured using a pendant drop of ink while the external phase consists of air. The volume of liquid in the pendant drop depends on the density and surface tension. The tensiometer employs edge tracing to capture and analyze the drop dimensions and determine the dimensionless quantity, H.

$$H = \frac{D_e}{D_s} \qquad (7)$$

H is then used to determine the surface tension using:

$$\gamma = \frac{\Delta\rho g\left({D_e}^2\right)}{H} \qquad (8)$$

where Δρ is the difference in density between the ink and air, g is acceleration due to gravity, De is the maximum drop diameter, and Ds is the drop diameter measured at a distance De from the drop apex, as shown in Figure 8 below. [21], [22].

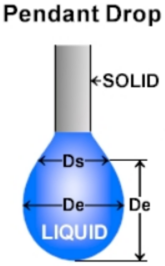

Figure 8. Geometry of pendant drop for measurement of surface tension.
[http://www.ramehart.com/surface_tension.htm]

The viscosity of the ink was measured using a rheometer (TA Instruments HR-2 Discovery). The measurements were done immediately after the ink was prepared according to the manufacturer's recommendation (i.e. shaking or bottle rolling, filtering, etc.). Viscosity of ink was measured over a range of shear rates from 10^{-3} to 10^{3} s^{-1}, with the low shear rate being representative of ink being slowly fed to the printhead from a reservoir, and the high shear rate being representative of ink being jetted at kHz frequencies. The viscosity of ink was measured over a range of temperatures from 20 to 50 °C, representative of inkjet nozzle temperatures and substrate temperatures. Each viscosity was measured twice to ensure that it was repeatable.

Contact angles were measured using a sessile drop, which is when a drop of liquid is produced and placed on the solid. The angle that is formed between solid/liquid and liquid/vapor interface is referred to as contact angle. The contact angles were measured geometrically using Rame-Hart tensiometer/goniometer. The software has an edge detection capability, and the contact angle is measured using the formula shown below [23]:

$$\theta = arctan\frac{b/_2}{r-h} \qquad (9)$$

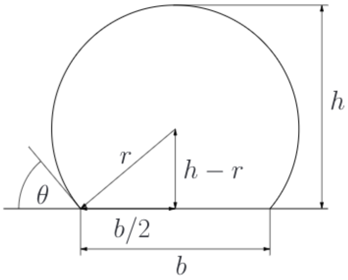

Figure 9. Geometrical measurement of the contact angle[23].

Contact angles were measured for 10 uL drops at 25 °C, which are the smallest that can be easily produced using a pipette and can be easily measured using the goniometer. The contact angles were measured on as-received substrates, and on substrates that were wiped with isopropanol (IPA), which is a common cleaning procedure.

3.4. Results and Discussion

3.4.1. Surface Tension Measurements of Ink

The purpose of this measurement is to investigate the printability of the chosen ink, and also to test the stability of the ink by measuring whether the surface tensions of the ink change over time (9 hours). The surface tension of each ink was measured initially, immediately after the ink was prepared according to the manufacturer's recommendation (bottle rolling and filtering). The ink was then kept at room temperature for 9 hours (similar to ink sitting in a printer reservoir), and the surface tension was then measured again. The results of the surface tension measurement is shown in Figure 10. The surface tension of Dupont PE410 did not change significantly over 9 hours.

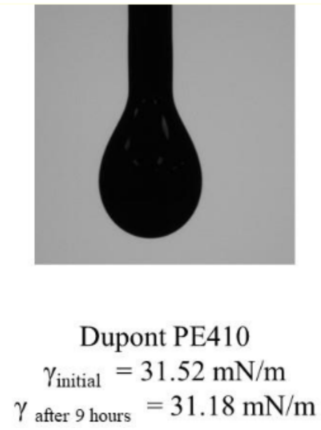

Figure 10. Surface tension of silver ink at 22 °C (initial, and after 9 hours at room temperature).

3.4.2. Viscosity Measurement of Ink

The purpose of this measurement is to investigate the printability of the ink, and also to test the stability of the ink by measuring whether the viscosity of the ink change over time (9 hours). The viscosity of the ink was measured initially, immediately after the ink was prepared according to the manufacturer’s recommendation (bottle rolling and filtering). The ink was then kept at room temperature for 9 hours (similar to ink sitting in a printer reservoir), and the viscosity was then measured again. Viscosity of ink was measured over a range of shear rates from 10^{-3} to 10^{3} s^{-1}, with the low shear rate being representative of ink being slowly fed to the printhead from a reservoir, and the high shear rate being representative of ink being ink-jetted at kHz frequencies. Viscosity of ink was measured over a range of temperatures from 20 to 70 °C, representative of inkjet nozzle temperatures and substrate temperatures. Each viscosity was measured twice to ensure that it was repeatable. The results of the viscosity measurements are shown in Table 2. The ink showed shear-thinning behavior (lower viscosity at higher shear rate). The viscosity of the ink decreased with increasing temperature at every shear rate. The viscosity of the ink did not change significantly over 9 hours.

Temp.	**η at 27 s^{-1}**	**η at 1000 s^{-1}**	**η at 27 s^{-1} after 9 hours**	**η at 1000 s^{-1} After 9 hours**
20ºC	60.1 cP	20.3 cP	60.1 cP	19.8 cP
30ºC	55.8 cP	15.9 cP	54.6 cP	15.7 cP
40ºC	52.4cP	12.7 cP	51.1 cP	12.5 cP
50ºC	50.8 cP	10.6 cP	49 cP	10.3 cP
70ºC	50.6 cP	9.21 cP	50 cP	9 cP

Table 2. Viscosity measurements on DuPont PE410 silver particle ink.

3.4.3. Contact Angle of Ink on Substrate

We have measured contact angles for 10 uL drops, which are the smallest that can be easily produced using a pipette and can be easily measured using the goniometer. However, we are aware that contact angle may increase as drop diameter decreases as a result of line tension, especially for drops with contact diameters of 10 µm and less [24]. Therefore, while 10 uL drops are likely to show trends among ink and substrates, they may not be accurate measurements of the contact angles of the 4 pL inkjet drops themselves. The measurements of the contact angles for 10 uL drops of Dupont PE410 at 25 °C are summarized in Table 3. Each measurement is the average of five separate measurements at separate locations. The contact angles are measured on as-received substrates, and also on substrates that were wiped with isopropanol (IPA), which is a common cleaning procedure. Goniometer images for Dupont PE410 on PET ST-505 are also shown as an example in Figure 11.

Substrate	**Ink**	**Contact Angle θ for $10\mu L$ Ink**
PET-ST505 (As received)	Dupont PE410	7.9°
PET-ST505 (Wiped With IPA)		7.7°
Dupont Kapton 500FN131 (As received)		60.7°
Dupont Kapton 500FN131 (Wiped With IPA)		63.4°
FEP (As received)		49.1°
FEP (Wiped With IPA)		57.1°

Table 3. Measured Dupont PE410 contact angles (10 µL volume) on the chosen substrates.

Figure 11. Goniometer images for the smallest and largest contact angles.

3.4.4. Printability of Ink

Here we will use density and the measured values for viscosity, surface tension of the ink to find the *Re* and *We* numbers and investigate the printability of it. Table 4-8 show the measured values and the corresponding *Re*, *We, Oh and Z* numbers that are calculated using equations 1-3 over a range of temperatures from 20 to 70 °C.

Ink	Density(g/cm^3)	Viscosity-20^{o}C(cP,mPa.s,g/m.s)	Surface Tension(mN/m,gm/s^2)	Re	We	Oh	Z
Dupont PE410	1700000	20.3	31.52	9.61	59.3	0.8	1.25

Table 4. *Re*, *We, Oh and Z* numbers calculated from viscosity and surface tension measured at 20^{o}C.

Ink	Density(g/cm^3)	Viscosity-30^{o}C(cP,mPa.s,g/m.s)	Surface Tension(mN/m,gm/s^2)	Re	We	Oh	Z
Dupont PE410	1700000	15.9	31.52	12.27	59.3	0.62	1.61

Table 5. *Re*, *We, Oh and Z* numbers calculated from viscosity and surface tension measured at 30^{o}C.

Ink	Density(g/cm^3)	Viscosity-40^{o}C(cP,mPa.s,g/m.s)	Surface Tension(mN/m,gm/s^2)	Re	We	Oh	Z
Dupont PE410	1700000	12.7	30	15.4	62.3	0.51	1.96

Table 6. *Re*, *We, Oh and Z* numbers calculated from viscosity and surface tension measured at 40^{o}C.

Ink	Density(g/cm^3)	Viscosity-50^{o}C(cP,mPa.s,g/m.s)	Surface Tension(mN/m,gm/s^2)	Re	We	Oh	Z
Dupont PE410	1700000	10.6	29.1	18.4	62.2	0.42	2.38

Table 7. *Re*, *We, Oh and Z* numbers calculated from viscosity and surface tension measured at 50^{o}C.

.

Ink	**Density(g/cm^3)**	**Viscosity-70°C(cP,mPa.s,g/m.s)**	**Surface Tension(mN/m,gm/s^2)**	**Re**	**We**	**Oh**	**Z**
Dupont PE410	1700000	9.21	28.8	21.2	64.8	0.37	2.7

Table 8. *Re*, *We, Oh and Z* numbers calculated from viscosity and surface tension measured at 70°C.

Based on the calculated values for Z, Dupont PE410 is printable over the range of 20-70 °C. Using equations Re, and We, the acceptable range for drop formation is shown on the map in Figure 12.

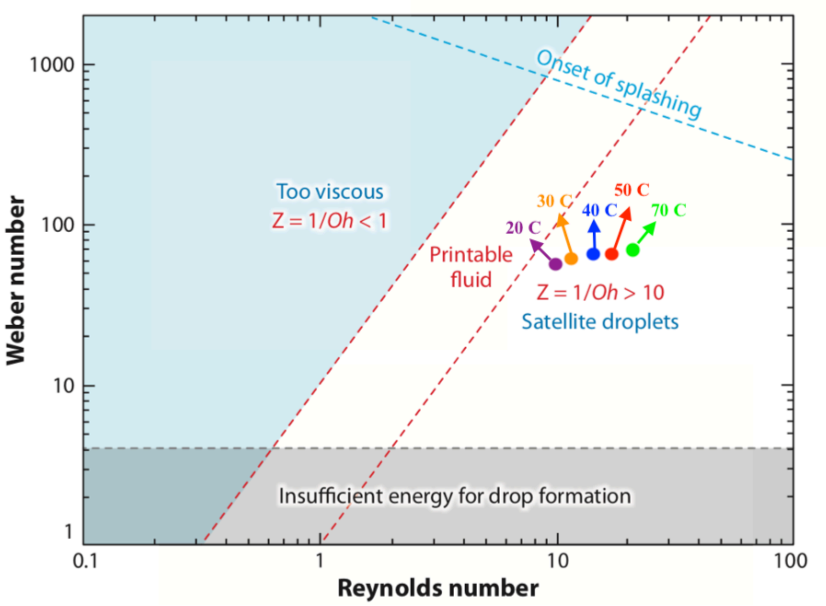

Figure 12. Acceptable drop formation of Dupont PE410 on drop formation map at various temperatures.

Based on Figure 12, Dupont PE410 at temperatures from 20 to 70 °C is printable; however, the points are slightly in the satellite droplets region. Figure 14 shows the dropview images (recorded by dropview camera of the printer) of PE410 ink being successfully jetted from the KM512-SH printhead. The jetted droplets have a long tail (slight satellite drop) which coalesces with the jetted droplet before it hits the substrates.

3.4.5. Jetting Parameters

The jetting waveform of the KM512-SH inkjet nozzles is determined by parameters as shown in Figure 13. The optimization of these parameters (settings) results in the jetting of stable single drops with desired drop velocity and without the occurrence of satellite droplets, spraying, accumulation of ink on the nozzle plate, or other such undesirable phenomena. The printer is able to apply the waveform settings and temperature to the printhead as expected. Optimized jetting settings for Dupont PE410 were determined and are shown in in Table 9.

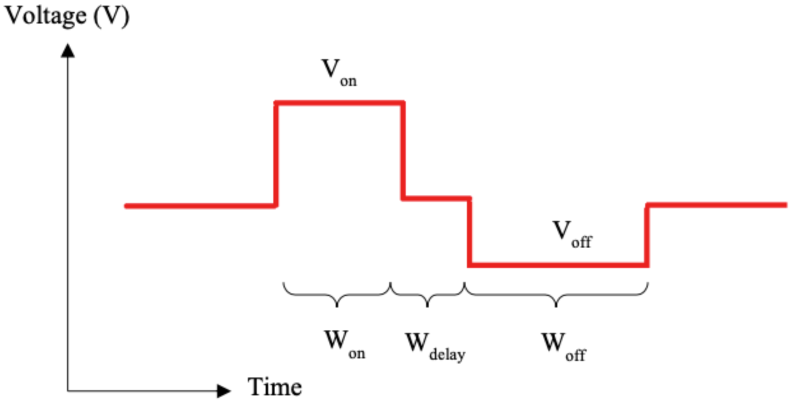

Figure 13. Jetting waveform of KM512-SH inkjet nozzles, and corresponding parameters.

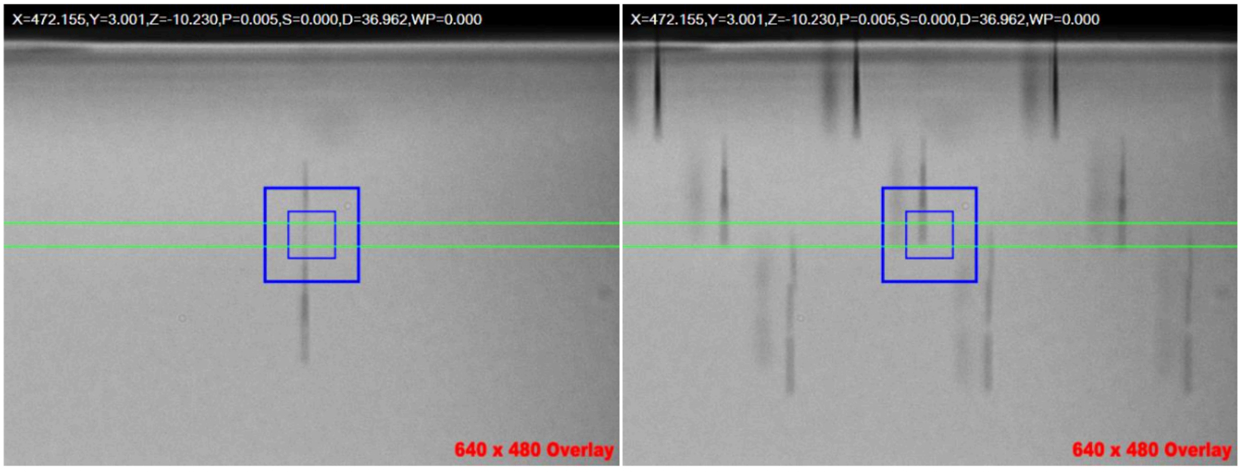

Figure 14. Dropview images of PE410 ink being successfully jetted from the KM512-SH printhead using waveform settings shown in table 8. Left side shows a single nozzle jetting, while the right side shows all nozzles jetting. In the image on the right, the darker, sharper drops are from the front row of nozzles (in focus), while the lighter, more blurry drops are from the back row of nozzles (out of focus).

DuPont PE410 on KM512-SH Printhead						
V_{on} (V)	V_{off} (V)	W_{on} (µs)	W_{delay} (µs)	W_{off} (µs)	T_{nozzle} (°C)	Backpressure Vacuum (mbar)
13	6.5	3	0	6	50	-26

Table 9. Jetting waveform settings provided by Dupont for PE410 ink on the KM512-SH printhead.

3.4.5. Effect of drop spacing and contact angle on print resolution

To investigate the effect of contact angle on print resolution, 1 pixel-width lines were printed with 1080 DPI (drop spacing of 24 µm) at 30°C. Based on the microscope images of these prints that are shown in Figure 15, the printed trace on PET ST505 is wider than that of Kapton FN. This correlates with PE410 having lower contact angle on PET ST505, the ink will spready more, compared to Kapton FN. Accordingly, as the contact angle increase, the print resolution enhances. However, as mentioned in section 3.1, other print parameters such as drop spacing and substrate temperature should also be considered because a combination of print parameters and ink/substrate interaction affect print resolution.

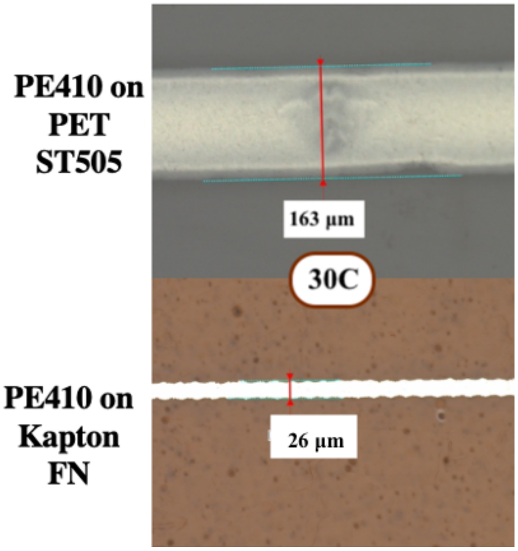

Figure 15. Effect of contact angle on line width/print resolution;1-pixel printed traces of Dupont PE410 on PET ST505 and Kapton FN.

To investigate the effect of drop spacing on print resolution, we printed 1-pixel lines on IPA- wiped PET ST505 at 50°C with various drop spacings. Figure 16 shows the microscope images of the printed lines. Based on the measured contact angles, the contact angle of PET410 on PET ST505 is 7.7°. Using equation 6 provided in section 3.1, the calculated printed drop diameter should be about 80 µm. The printed line with 97.5 µm drop spacing confirms the calculated diameter. As the drop spacing decreases, the drops will start to coalesce and when the overlap of adjacent drops is close to 50% or half of individual dried printed drop diameter (drop spacing of 40 µm), continuous traces with smooth edges can be printed. As the drop spacing is further decreased and it gets too small (drop spacing of 7 µm), bulging starts to appear.

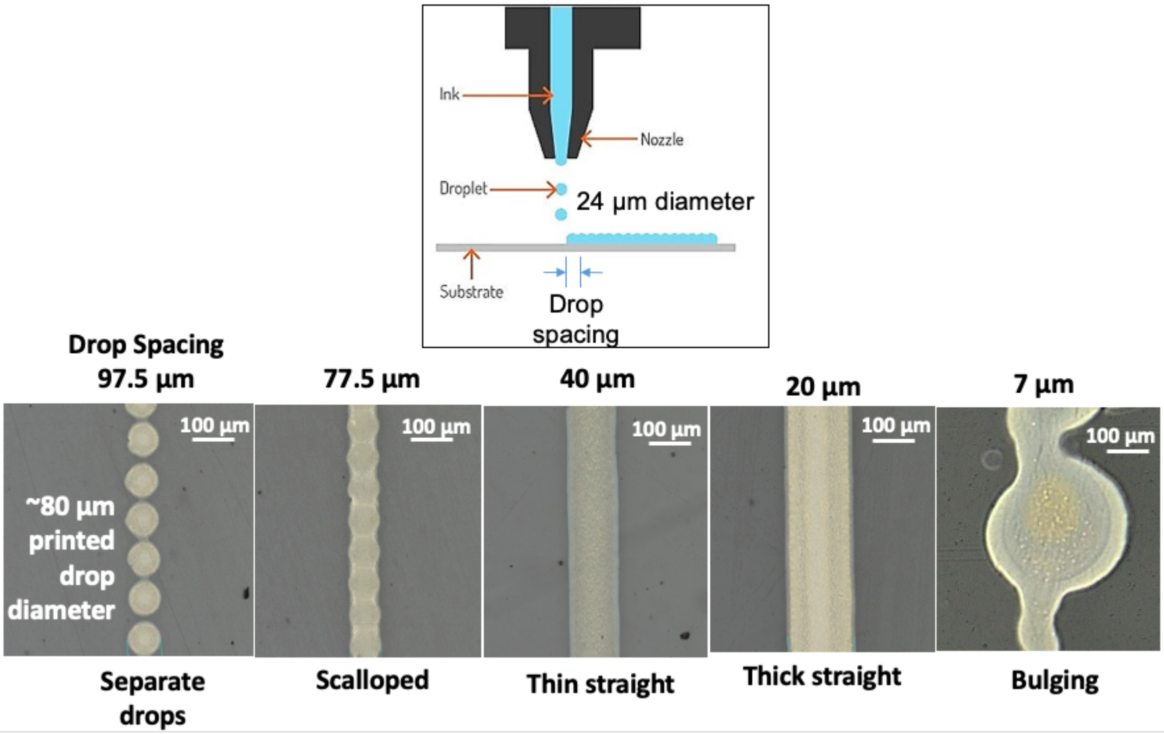

Figure 16. Effect of drop spacing on print resolution/line width; 1-pixel printed traces of Dupont PE410 on PET ST505 with various drop spacing.

3.4.6. Effect of substrate temperature on print resolution

To investigate the effect of substrate temperature on print resolution, a set of print experiments was undertaken for Dupont PE410 on PET ST505 (low contact angle substrate) and Kapton 500FN131 (high contact angle substrate) substrates. For these set of experiments, 1 pixel-width lines were printed with 1080 DPI (drop spacing of 24 μm) at 30°C, 50°C, and 70°C substrate temperature. Figure 17 shows the microscope images, trace width and cross-section profile of these prints on PET ST505.

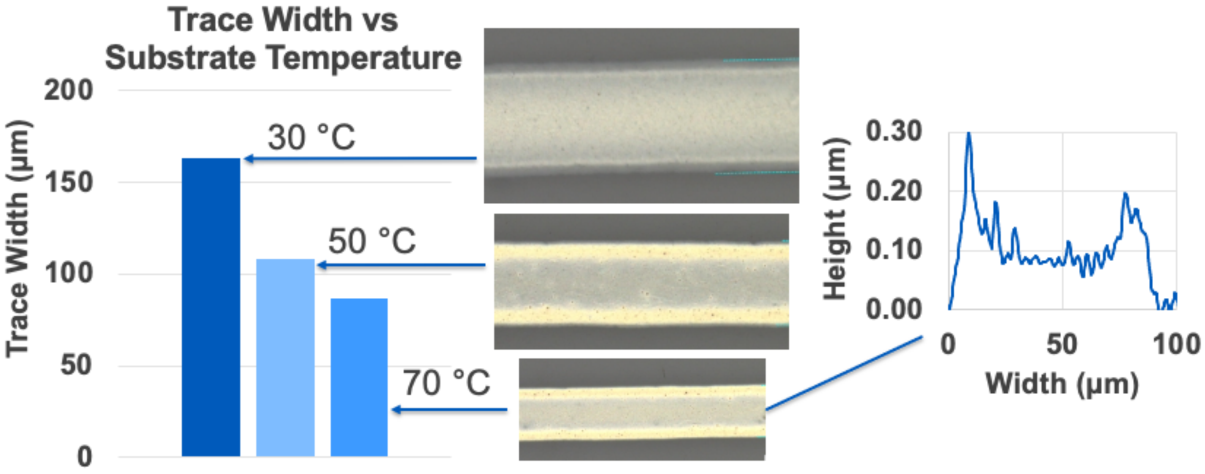

Figure 17. Printed traces of Dupont PE410 on PET ST505 at 30°C, 50°C, and 70°C with drop spacing of 24 μm.

Based on these microscope images, trace width decreases as substrate temperature increases which is due to faster drying at higher temperatures and pinning of contact lines which prevents the ink from spreading at higher temperatures. Based on the cross-section profile, the traces are thicker toward the edges and thinner in the middle which is due to faster flow of the ink toward the edges of the trace at higher temperature. This type of deposition pattern is called coffee ring effect. Having smoother edges and eliminating coffee ring effect is an area of interest for research conducted in printed electronics [25]

The same set of print parameters was used to print PE410 on Kapton FN at 30°C, 50°C, and 70°C substrate temperature and the microscope images of the traces are shown in Figure 18.

Unlike PET ST505, we can see that for Kapton FN when substrate temperature increases, the ink balls up into discontinuous patches rather than forming a continuous trace. This means that the ink can dewet the substrate or in other words that PE410 has a non-zero receding contact angle on Kapton FN. Receding contact angle is the lowest measurable contact angle when the contact line of the droplet recedes[26]. In Chapter 6 we will address this balling up issue and talk in detail about how receding contact angle can be measured. The difference in how print resolution is affected by increasing substrate temperature for Kapton FN vs PET ST505 emphasizes the importance of the need for optimizing all print parameters and not just relying on one parameter when studying print resolution.

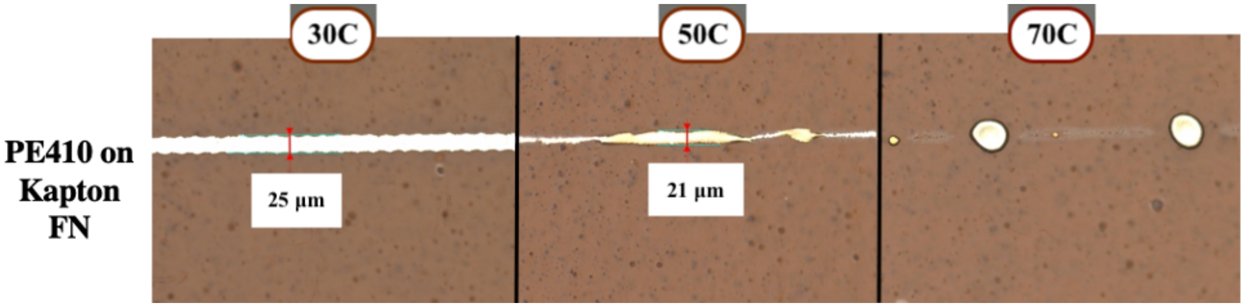

Figure 18. Printed traces of Dupont PE410 on Kapton FN at 30°C, 50°C, and 70°C with drop spacing of 24 µm.

So far, the best print resolution that we achieved was for a 1 pixel-width lines of PE410 on PET ST505 printed with 1080 DPI (drop spacing of 24 µm) at 50°C substrate temperature. However, we showed that by further increasing substrate temperature to 70°C, we could achieve higher print resolution for PE410. So, we printed 1 pixel-width line of PE410 on PET ST505 with 1080 DPI (drop spacing of 24 µm) and 70°C substrate temperature. The microscope image of the printed trace with optimized print parameters is shown in Figure 19. The microscope image confirm enhancement in print resolution since the line width decreased from 86 µm to 63 µm.

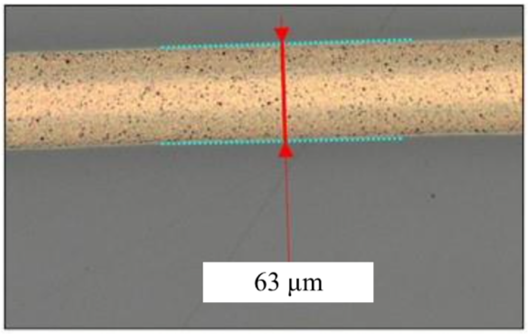

Figure 19. 1-pixel printed trace of Dupont PE410 on PET ST505 at 70°C with drop spacing of 24 μm.

Based on these results, the narrowest 1-pixel trace that could be printed in a single print pass on PET ST505 is around 63 μm in width. To further enhance print resolution, we will physically modify the surface of PET ST505 by patterning them with microfeatures and microchannels using nanoimprint lithography and will study the effect of these physical modifications on print resolution (Chapters 4 and 5). Also, we will chemically modify the surface of Kapton FN, and will study its effect on the print resolution and the discontinuity that we observed in printed traces on Kapton FN at higher substrate temperatures (Chapter 6).

Chapter 4

Nanoimprint Lithography (NIL) Patterned Surfaces for High-Resolution Inkjet Printing

4.1. Introduction

As mentioned in Chapter 3 (Equation 6), on a flat and smooth surface, the print resolution depends on the inherent contact angle of the ink on the substrate, the initial drop size, and the dynamic of drop coalescence. The print resolution can be tuned by controlling these factors. The other way that the print resolution can be controlled is through physically controlling the spread of the ink on the substrate, or by patterning the substrate and tuning its surface energy, which will again affect the spreading of the ink[17]. Sirringhaus et al. reported fabricating a fluidphobic stripe using a combination of photolithography and plasma etching of a polyimide film for arresting the drop spreading and controlling the inkjet printing resolution [27]. Other studies also reported enhancing drop resolution by printing drops onto a fluidphobic stripe and controlling print resolution through dewetting of the drop and creating smaller-width features [28], [29]. Although these methods are shown to be successful in enhancing the print resolution by physically controlling drop spread, there is lack of proof and study that they can also control dynamic instabilities associated with drop coalescence. The other disadvantage of these methods is that inkjet printing will not be purely digital because the substrates should be chemically-patterned in the same shape as the printed patterns.

As mentioned above, drop spread can also be controlled by patterning the surface and tuning surface energy of a substrate. The works most relevant in this regard are by Feng et al and priest et al [30], [31] [32]. In the work of Feng et al, an SU-8 surface with both primary micro-features and secondary nano-features on top of the primary micro-features was fabricated using electron beam lithography and subsequently modified with fluoroalkylsilane via a vapor-phase reaction. This geometry showed both high contact angle and high adhesion for water droplets. The high contact angle is a result of the high surface area created by the hierarchical micro- and nano-structures, while the high adhesion is due to the water droplets being in the Wenzel wetting state, in which the drop fully and conformally wets the entire structured surface (Figure 20). This is in contrast with the Cassie wetting state, in which the drop is in contact with only the tops of the features and air is trapped in between the features beneath the drop, in which case there is an even higher contact angle than in the Wenzel state, but very low adhesion, with a tendency for drops to bounce and roll on the surface.

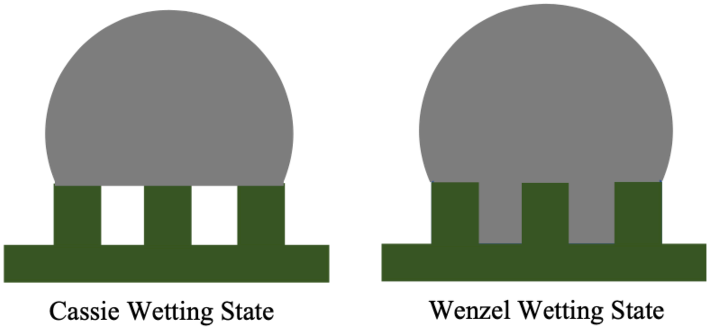

Figure 20. Drops in either Cassie or Wenzel wetting state on micro- or nano-structured surface.

Priest et al. investigated the spreading of a liquid in square micropillar arrays with various geometries. The pillars were made in SU8 using UV-photolithography. The width of the pillars was kept constant at 20 μm while the height varied from 2 to 30 μm. They showed that for short micropillars and low area fraction, the contact line of the droplet will pin while for tall pillars and high area fraction, the frontline of the drop will advance till the whole volume of the droplet is consumed [30]. In another study they showed that by increasing micropillar density, the advancing contact angles reached that of a superhydrophobic surface (140°) while the liquid was in Wenzel state. This high advancing contact angle cannot be explained by Cassie State or Wenzel law since the inherent contact angle of their material was less than 90°. Using simulations, they showed that for short micropillar with higher pillar density, the high contact angle was due to contact line pinning which was confirmed by microscope images [31].

The Wenzel wetting state is preferred for ink drops in our study because this is more likely to lead to the formation of continuous conductive traces, while the Cassie wetting state may result in conductive ink being deposited discontinuously only on the tops of the features. Other studies have shown that increasing the velocity of drop impact on the surface, pushing the drop into the surface, or increasing the temperature of the drop can all enable the drop to obtain the Wenzel wetting state, rather than the Cassie wetting state [33], [34].

4.2. Objectives and Scope

To the best of our knowledge, no study has investigated the effect of microfeatured surfaces on the inkjet resolution so far. In the present project, inkjet drops have velocities of several meters per second (~9.6 m/s) and can also be heated by the printhead. Therefore, there is a good chance that the ink will fully penetrate the area in-between the microfeatures if we inkjet print on a surface patterned with microfeatures. Therefore, we hypothesize that microfeatures will enhance formation of continuous traces. We also hypothesize that microfeatures will enhance print resolution through preventing ink spread. To investigate these hypotheses, we have the following objective:

1. Study the effect of microfeatures on print morphology and resolution through printing lines with various drop spacing and characterizing the printed lines using profilometry and microscope imaging
2. Study the effect of substrate temperature (drying) on print resolution
3. Study the electrical conductivity of the printed traces

4.3. Approach and Methods

In this study, we used Dupont PE410 silver conductive ink (Solvent-based, 45% Ag loading, 20-40 cP @ 25°C) as our conductive ink because of its high loading of silver nanoparticles and its compatibility with KM512-SH printhead. The substrates with microfeatures were provided by Carpe Diem Technologies using their R2R NIL system.

In the R2R NIL system, the roll of web is placed on to the unwind module's unwind tension roller. As the web is unwinding, it moves through a web cleaner that removes any particles from the substrate. Once cleaned, the web goes through a corona surface treatment module to increase web surface energy. As the surface energy increases, both coating adhesion and uniformity increases. The web is now ready for the micro gravure coating station. Once a uniform layer of coating is applied to the web, the web travels through a NIR (near infra-red) oven/unit to further improve coating uniformity. The next station is the nano imprint lithography (NIL) module. The NIL module is equipped with a nickel master that will replicate the features on to the oncoming coated web. A pinch roller will press the web onto the master ensuring proper replication. As the web travels on the master, a UV light source is applied to initiate the photo-initiators within the resin. Once the web has traveled past the UV source, the web is separated from the master by the stripping roller. The web should now have the features imprinted and is rewound by the rewinding roller.

For microfeatures, a height (H_m) of 1.236 µm, widths (W_m) of 1.236 and 2.472 µm, and spacings (S_m) of 2.472 µm have been chosen. Figure 21 shows a schematic of the design for NIL patterned surfaces. Bitmaps of the microfeatures for the nickel master were provided by WPI using MATLAB script which is shown in Figure 22.

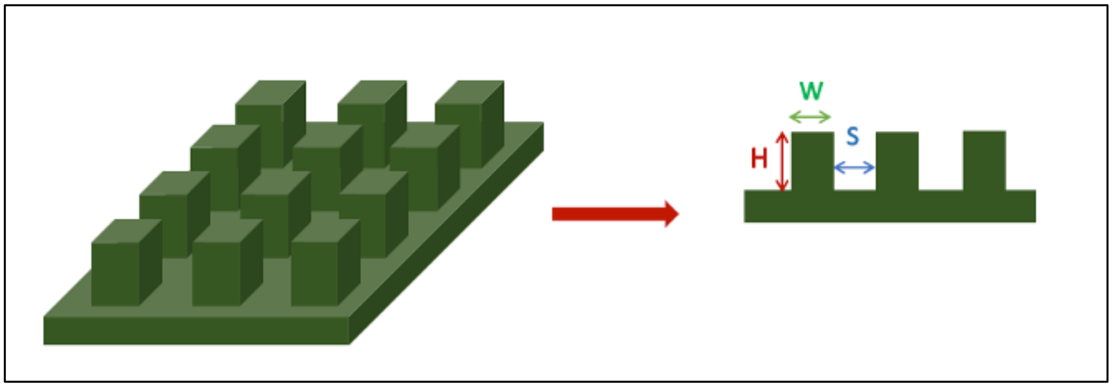

Figure 21. Schematic of design for NIL patterned surfaces to be printed onto by inkjet.

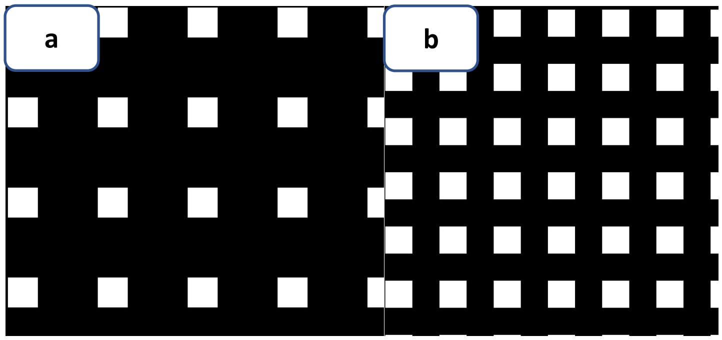

Figure 22. Bitmaps of (a) S= 2.472 (µm),W= 1.236 (µm) and (b) S= 2.472 (µm),W=2.472 (µm)

The coating, resin, used for the NIL process is Norland NOA 85. NOA 85 is a clear, liquid photopolymer that will cure when exposed to ultraviolet light. Curing time of this material is remarkably fast and it has low shrinkage and slight flexibility.

Contact angle was measured using Rame-Hart tensiometer/goniometer for 10uL drop of PE410 ink, which is the smallest that can be easily produced using a pipette. Keyence VHX-7000 microscope was used for imaging, and KLA Tensor AlphaStep D600 Stylus Profilometer was used for 2D profile measurement of the printed traces.

The 2-probe resistance of the traces was measured using a Hioki RM3545 resistance meter after the traces were annealed at 130°C for 30 minutes in a box furnace. Electrical connections to the traces were made using fine copper wire and Circuitworks CW2400 silver epoxy cured for 24 hours at room temperature.

4.4. Results and Discussion

4.4.1. Contact Angle of Ink

The contact angle for 10 μL drops of Dupont PE410 on NOA 85 is 32^o. The measurement is the average of five separate measurements at separate locations. A goniometer image for Dupont PE410 on NOA 85 is also shown in Figure 23.

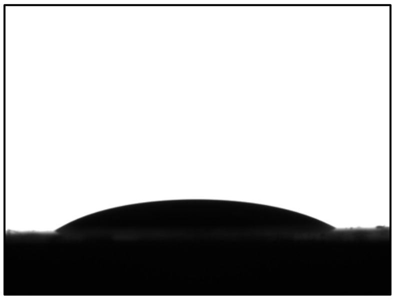

Figure 23. Goniometer images for the contact angle of Dupont PE410 on PET coated NOA 85.

4.4.2. Printed Traces on Microfeatures

1 pixel-wide traces on NOA 85, NIL microfeature patterned NOA 85 with width of 1.236 (μm) and 2.472 (μm) and spacing between features of 2.472 (μm) were printed at 70^oC substrate temperature. Drop spacings from 10 μm to 105 μm with 5 μm increment were used for printing 1-pixel lines. The goal for changing the drop spacing was to find the optimal drop spacing or a range of drop spacings for printing continuous lines with minimum width. The other goal was to investigate the effect of the microfeature on the morphology of the printed lines. The range of drop spacings was narrowed down to drop spacings from 10 μm to 45 μm because it was found that for drop spacings of more than 45 μm, we just had individual drops, and with increasing the drop

spacing, the drops just got further apart from one another and there was no change in the morphology of the printed drops. Figures 24, 25, and 26 show the printed lines on NOA 85, NIL microfeature patterned NOA 85 with width of 1.236 (μm) and spacing of 2.472 (μm), and NIL microfeature patterned NOA 85 with width of 2.472 (μm) and spacing of 2.472 (μm), respectively.

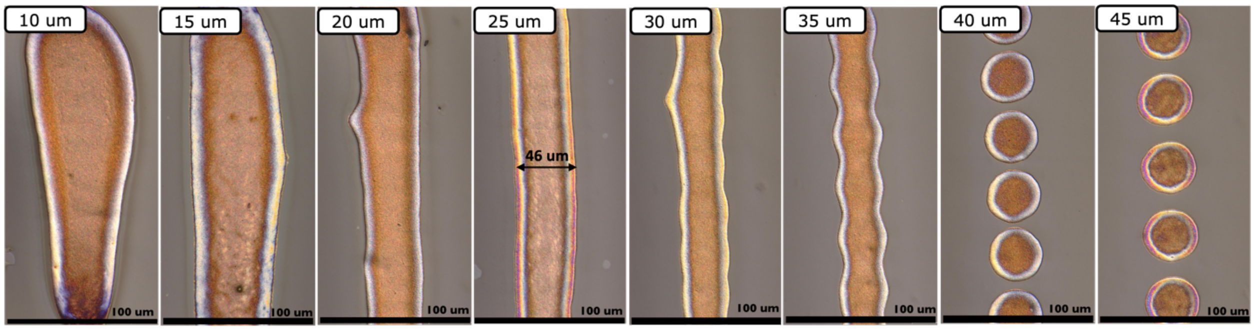

Figure 24. 1 pixel-wide traces printed at 70ºC on NOA 85 with drop spacing from 10 μm to 45 μm.

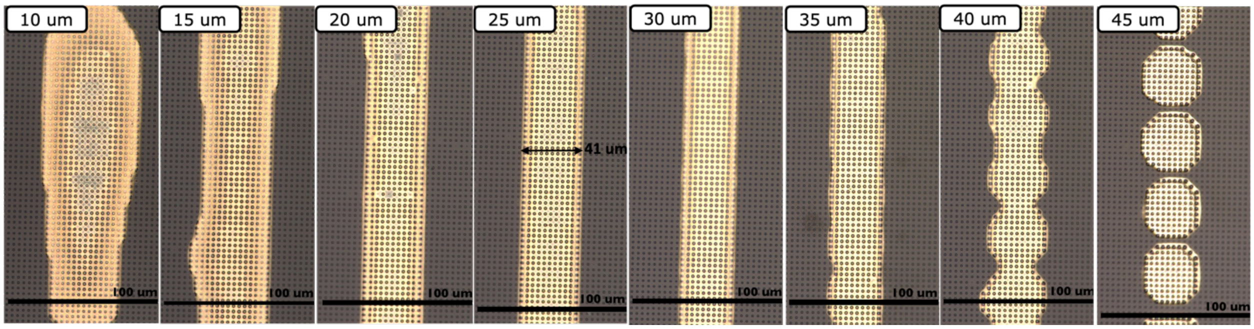

Figure 25. 1 pixel-wide traces printed at 70ºC on NIL microfeature patterned NOA 85 with width of 1.236 (μm) and spacing of 2.472 (μm) with drop spacing from 10 μm to 45 μm.

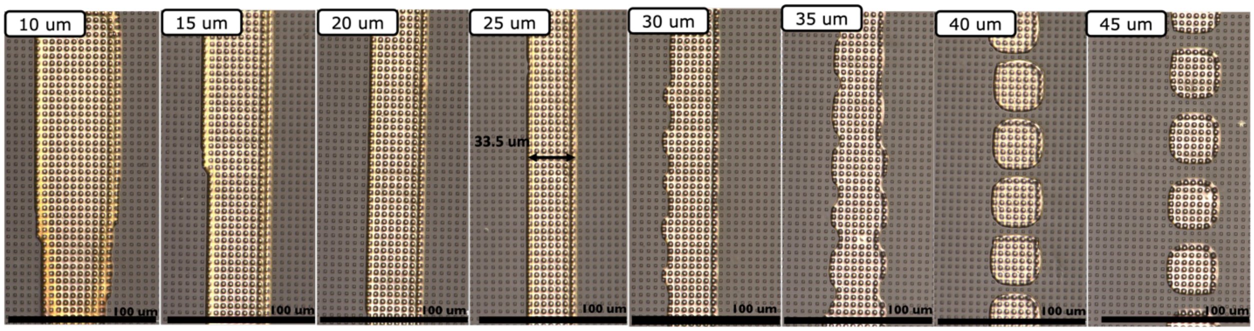

Figure 26. 1 pixel-wide traces printed at 70ºC on NIL microfeature patterned NOA 85 with width of 2.472 (μm) and spacing of 2.472 (μm) with drop spacing from 10 μm to 45 μm.

Compared to a flat surface, when having a surface with an array of features, which in our case is an array of microfeatures with defined geometry, the wettability of the surface will depend not only on the inherent contact angle of the material, but on the geometry, and the density of the features on the surface [30]. As it can be seen in Figures 24-26, the traces printed on the microfeatures resulted in narrower traces with smoother edges compared to the ones printed on NOA 85 with no microfeatures. For traces printed on NOA 85, only the trace printed with 25 µm drop spacing resulted in a line that has partially smooth, straight edges while for traces printed on microfeatures, for drop spacing range of 20-30 µm, the edges of the traces are smooth and straight, and this is due to the pinning of the ink along the rows and columns of the microfeatures array. The trace printed on NOA 85 with 25 µm drop spacing has the smallest trace width with minimum print instability, bulging, that is discussed in Chapter 3. The traces printed with 25 µm drop spacing on microfeature arrays, for both geometries, also show the smallest line width compared to other drop spacings; however, the line width for the traces printed on microfeatures are 41 µm and 33.5 µm which are 5 µm and 12.5 µm smaller than that of the trace printed on NOA 85 with no microfeature array, respecively. This confirms the hypothesis that the microfeatures act as a barrier against ink spread and thereby confine the ink to a smaller area compared to that of a flat surface with no microfeatures. This confinement occurs due to the pinning of the ink contact line. Comparing the two microfeature array geometries, the design with wider microfeature width (same spacing) introduces more barrier against ink spread and this is due to having higher density of microfeatures on the surface which is also confirmed in other studies [31]

Based on the measured contact angle and formula 6, the dried drop diameter should be about 41.6 µm, which is close to the measured line width for the trace printed with 25 µm drop spacing on NOA 85. The fact that line width of the printed lines with 25 µm drop spacing on microfeatures, for both geometries, is smaller than 41.6 µm confirms the confinement of the ink due to the presence of the features on the surface and it shows the effectiveness of microfeatures on print resolution, and edge definition of the printed lines.

In order to improve our understanding of the role of drying and substrate temperature on ink spread, we repeated the above-mentioned set of prints at 30°C. Figures 27, 28, and 29 show the printed lines on NOA 85, NIL microfeature patterned NOA 85 with width of 1.236 (µm) and spacing of 2.472 (μm), and NIL microfeature patterned NOA 85 with width of 2.472 (μm) and spacing of 2.472 (μm), respectively.

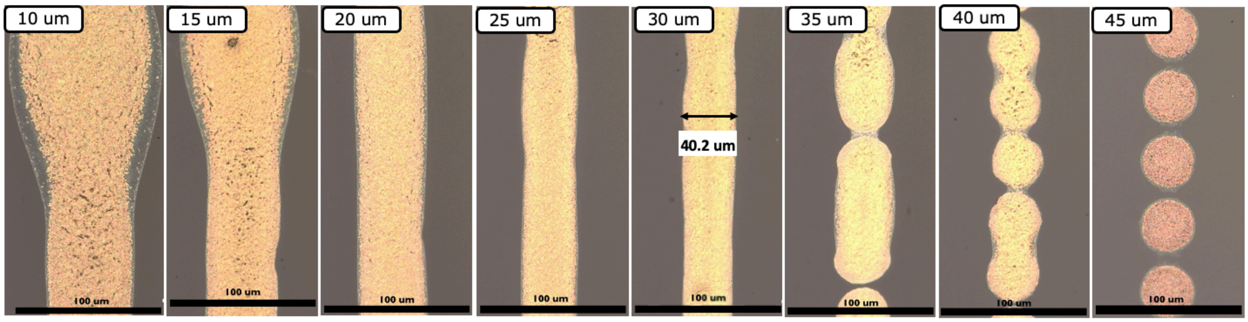

Figure 27. 1 pixel-wide traces printed at 30ºC on NOA 85 with drop spacing from 10 μm to 45 μm.

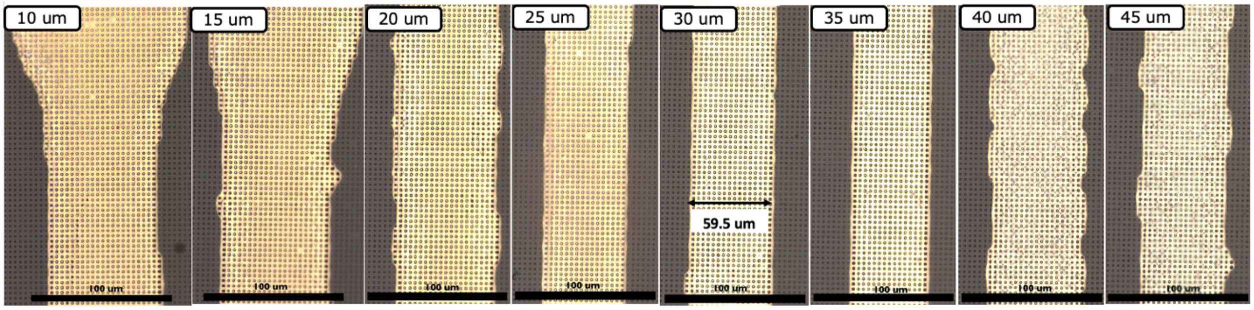

Figure 28. 1 pixel-wide traces printed at 30ºC on NIL microfeature patterned NOA 85 with width of 1.236 (μm) and spacing of 2.472 (μm) with drop spacing from 10 μm to 45 μm.

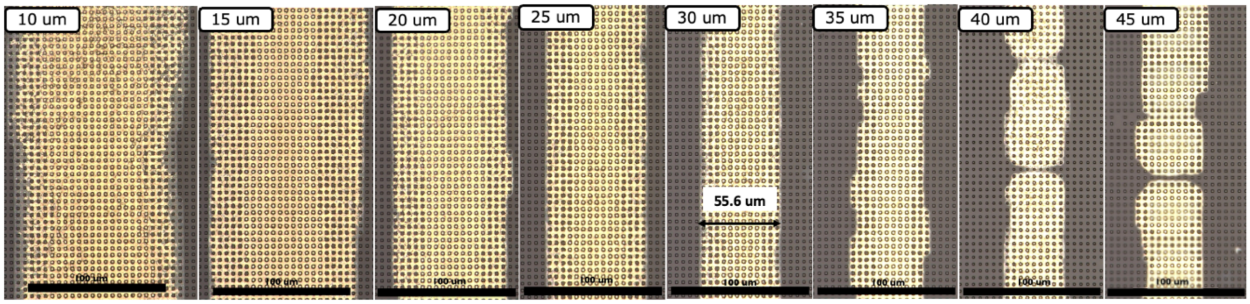

Figure 29. 1 pixel-wide traces printed at 30ºC on NIL microfeature patterned NOA 85 with width of 2.472 (μm) and spacing of 2.472 (μm) with drop spacing from 10 μm to 45 μm.

Figure 30 shows a comparison/summary of the traces with smallest width printed at 30ºC and 70ºC. Similar to the traces printed at 70ºC, for the traces printed at 30ºC on the two microfeature array geometries, the design with wider microfeature width (same spacing) introduces more barrier against ink spread. The traces printed on NOA 85 with no microfeature at both temperatures have similar trace width while the traces printed on NIL microfeature patterned NOA 85 at 70ºC have smaller traces width compared to the traces printed at 30ºC. This shows that the smaller width of the traces printed at 70ºC on NIL microfeature patterned NOA 85 is not only due to the presence of the microfeatures, but it is due to higher substrate temperature and higher drying rate of the ink which contributes to the pinning of the contact line along the array of microfeatures.

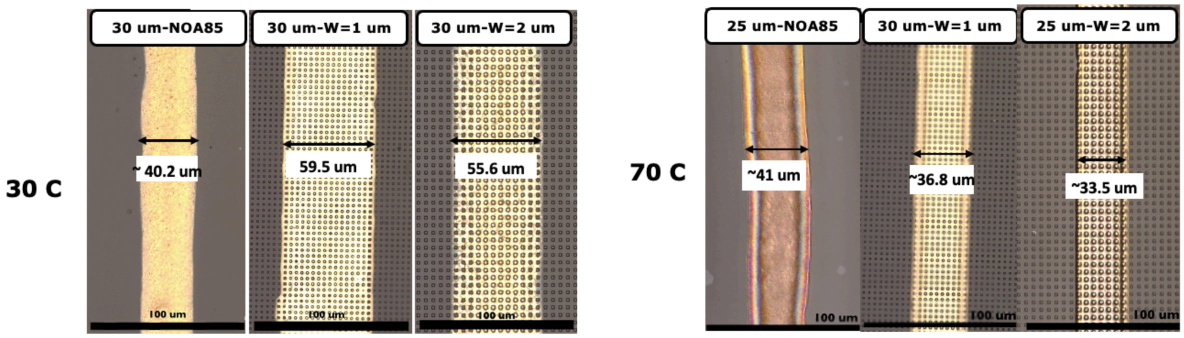

Figure 30. Side-by-side comparison of the traces with smallest width printed at 30ºC and 70ºC.

The print parameters for the trace with the smallest width, 1 pixel-wide traces printed at 70ºC on NIL microfeature patterned NOA 85 with width of 2.472 (μm) and spacing of 2.472 (μm) with drop spacing of 25 μm, was chosen for printing multiple passes/layers, without permitting the previous passes to dry in order to increase conductor thickness. As a comparison, multiple passes were printed on NOA 85 at 70ºC with drop spacing of 30 μm which are the print parameters that resulted in the smallest trace width printed on NOA 85. Figure 31a and 31b show traces printed up to 4 layers thick on NIL microfeature patterned NOA 85 with width of 2.472 (μm) and spacing of 2.472 (μm) and NOA 85, respectively. The main takeaways are that for the printed traces on NIL microfeature patterned NOA 85, for 1-2 layers, the trace width does not seem to increase by adding a second layer on top of the first printed layer, which can be confirmed by the obtained profiles of the 1-2 layers traces using the profilometer shown in Figure 31c. However, for more than 2 layers, bulging in the traces appears. Also, for the traces printed on NOA 85, for more than one layer, there is spill over and bulging in traces. So, microfeatures not only enable us to have higher print resolution of traces that are one layer but to have higher thickness of conductors (up to 2 layers) with acceptable resolution. The other noticeable difference between the traces printed on NIL microfeature patterned NOA 85 and on NOA 85 with no pattern is that for the traces that are printed on flat NOA 85, there is more deposition toward the edges of the trace compared to the center of the trace (coffee ring deposition pattern).

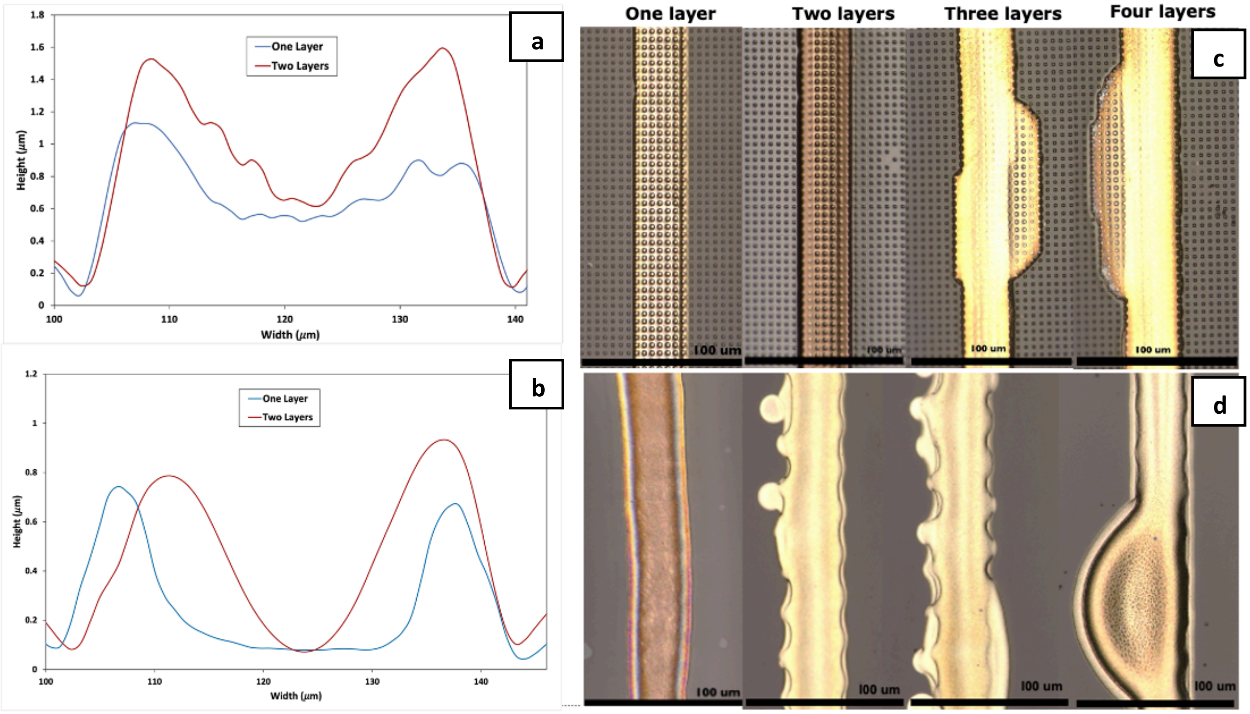

Figure 31. (a) Profilometer profiles of 1-2 layers of 1 pixel-wide traces printed at 70°C on NIL microfeature patterned NOA 85 with width of 2.472 (μm) and spacing of 2.472 (μm). (b) Profilometer profiles of 1-2 layers of 1 pixel-wide traces printed at 70°C on NOA 85, (c) 1-4 layers of 1 pixel-wide traces printed at 70°C on NIL microfeature patterned NOA 85 with width of 2.472 (μm) and spacing of 2.472 (μm), and on (d) NOA 85

The resistance of 1-2 layers of 1 pixel-wide printed traces both on NOA 85 and on NIL microfeature patterned NOA 85 with width of 2.472 (μm) and spacing of 2.472 (μm) was measured after annealing for 30 minutes at 130°C. The results are shown in Figure 32. Based on the measured resistances, for traces with 2 layers, the resistance is less than that of a trace with one layer both for the printed traces on NOA 85 with and without patterns which is due to the presence of more of the conductive material, silver nanoparticles. The resistance of the traces printed on NIL microfeature patterned NOA 85 is very close to that of the traces printed on flat NOA 85 both for 1 and 2 layers of printed traces which shows that the micropillars do not have a negative effect on the conductivity and the traces printed on NIL microfeature patterned NOA 85 are continuous.

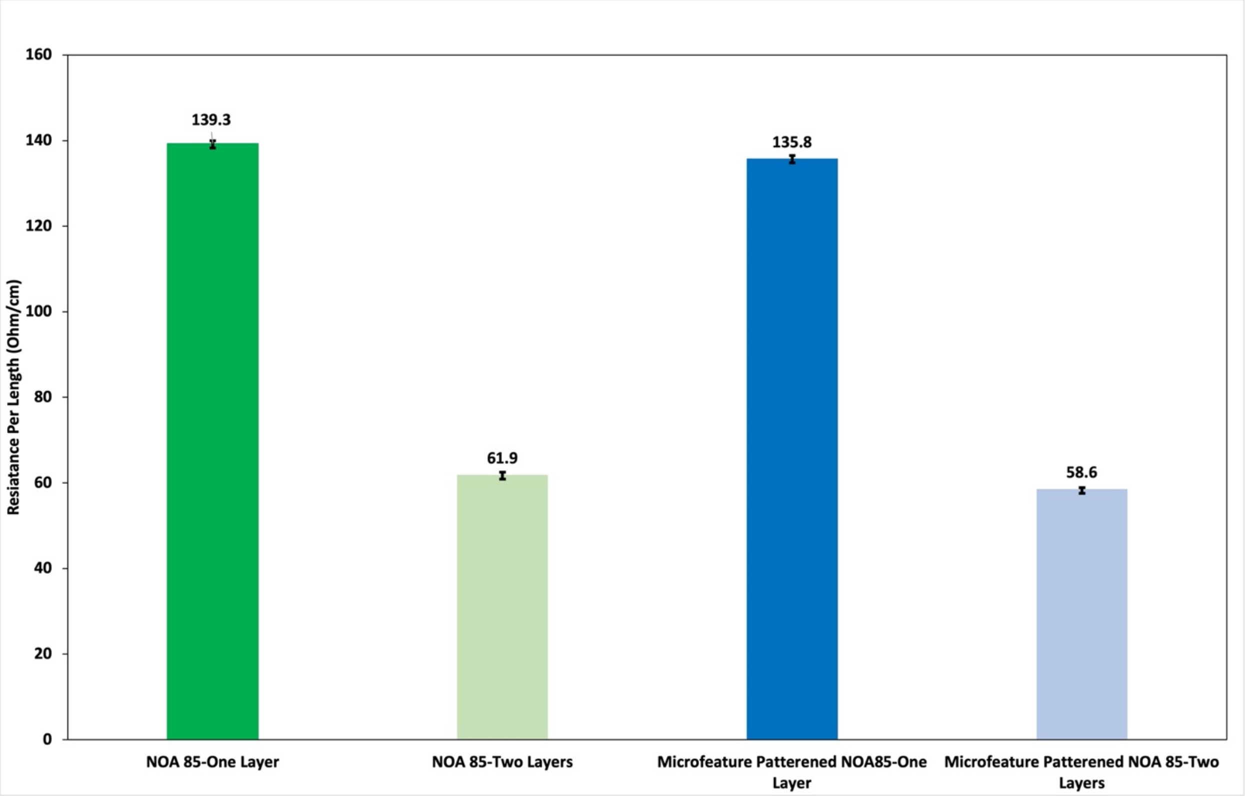

Figure 32. Resistance per unit length of 1-2 layers of 1 pixel-wide printed traces both on NOA 85 and on NIL microfeature patterned NOA 85 with width of 2.472 (μm) and spacing of 2.472 (μm).

4.5. Conclusions

A combination of NIL microfeature patterning with optimized geometry and printing at elevated temperature was used to enhance print resolution. Here, it is shown that print resolution of printed traces up to 2 layers thick was successfully enhanced (width was decreased) by printing on a microfeature patterned surface at 70^{o}C. Enhancement in the profile of print deposition toward the edges of the printed traces compared to the center of the trace is also shown, decrease of coffee ring effect, for both 1 and two layers of printed traces. By measuring the resistance of the printed traces on NIL patterned surfaces, it is proved that the traces are continuous and that the micropillar patterns did not have a negative effect on the continuity or electrical resistance of the trace.

Chapter 5

Nanoimprint Lithography (NIL) Microchannels for High Resolution Inkjet Printing

5.1. Introduction

As mentioned in previous chapters, on a flat and smooth surface, the print resolution depends on the inherent contact angle of the ink on the substrate, the initial drop size, and the dynamic of drop coalescence. In the field of printed electronics, it is very important to control ink spreading for two reasons:

- The ink spread will place an upper limit on the print resolution. This is especially important for printing fan outs for surface mount of packaged and unpackaged ICs having high pin/bump count with small pitch between pins/bumps.

- The ink spread will make it hard to print thick and narrow features (i.e. having high aspect ratio). Thicker and narrower features are desired to simultaneously achieve high electrical conductance and small area footprint. This is especially important for conductive traces that need to carry high currents.

To address the above-mentioned drawbacks, we propose a surface having microchannels imprinted into Norland 85 coated PET sheets by nanoimprint lithography (NIL). Dupont PE410 will be printed along the entire length of the microchannel. The walls of the microchannel confine the ink and prevent it from flowing outwards, resulting in feature shape and size that is tightly controlled by the microchannels. The work that is most closely related to our study is by Mahajan et al[35]. In this study microchannels and reservoirs were created by imprinting a stamp into a PET substrate coated with a curable epoxy prepolymer. The coating was solidified by UV illumination, and the stamp was peeled off. The resulting microchannels and reservoirs had ink-philic walls and floor. A particle-free silver ink was then ink-jetted into the reservoirs, and wicked into the microchannels by capillary action. This study showed that ink travel length in the microchannels is determined by a competition between wetting speed and drying time and is a function of both the ink properties and channel cross-section dimensions. Increasing channel depth increases the ink travel length and the conductivity of the resulting traces. Increasing the channel width also increases conductivity, but there is an optimum value of width for achieving maximum ink travel length, with smaller widths causing too much frictional flow resistance and larger widths creating less capillary action. Travel lengths of up to 6 mm were achieved for channel depth of ~20 μm and channel width of ~ 10 μm. The filled microchannels in this study had relatively thin coatings of silver that coated the walls of the microchannels but did not fill it. The silver was used to electroplate copper to achieve filling of the microchannels.

In the present project, however, the goal is to fill the whole length of microchannels and to print multiple layers of the ink using inkjet printer so that we are not relying on capillary action for filling the microchannels. This will be important for achieving high trace conductance, and also important for die- attach, which requires a trace that is at least flush with the substrate or preferably protrudes from it. The ink will fill the microchannels if the floor and walls of the microchannel are receptive to the ink, i.e. if there is a sufficiently low ink contact angle with the floor and walls. Sufficient velocity and/or pressure of the ink can also facilitate filling of the microchannels.

5.2. Objectives and Scope

As mentioned above, the hypothesis is that walls of the microchannel confine the ink and prevent it from flowing outwards, resulting in feature shape and size that is tightly controlled by the microchannels. Hence it will enhance print resolution and facilitate printing traces with higher thickness. Multiple layers of ink can also be printed into the microchannel, to fill it to the desired depth. The ink is allowed to dry partially or completely in the microchannel between printing of successive layers. Printing at an elevated substrate temperature can accelerate the drying of the ink and enable fast filling of the microchannels by multiple printed layers, so we plan to print inside microchannels at 70ºC. To investigate these hypotheses, we will study the effect of microchannel on print resolution using optical microscope imaging. We will also investigate the trace thickness and cross section profile of it using optical profilometry.

5.3. Approach and Methods

In this study, Dupont PE410 silver conductive ink (Solvent-based, 45% Ag loading, 20-40 cP @ 25°C) was used as conductive ink because of its high loading of silver nanoparticles and its compatibility with KM512-SH printhead. The substrates with microchannels were provided by Carpe Diem Technologies using their R2R NIL system, detailed description this system is provided in Chapter 4.

For microchannels, width of 40 µm, length of 1mm and depth of ~4 µm (due to manufacturing constraint) have been chosen. Microchannels were designed using SolidWorks software. The design also includes triangle marker at a specific distance from the microchannels to make locating microchannels and also print alignment easier. Figure 33 shows a schematic of the design of the microchannels.

Figure 33. Schematic of microchannels geometry.

Keyence VHX-7000 microscope was used for imaging, and KLA Tencor AlphaStep D-600 Stylus Profilometer was used for profile measurement of the printed traces inside the microchannels.

5.4. Results and Discussion

5.4.1. Preliminary Results

Optimized jetting settings used for Dupont PE410 for printing inside microchannels are same as parameters used in section 4.4.2.

1-4 layers of 1 pixel line of silver ink was printed into microchannels that are nominally 40 µm wide and ~4 µm deep. The print settings were 70 °C substrate temperature, ~2520 DPI (10 µm drop spacing), 1000 Hz jetting frequency.

Figure 34 shows the microscope image, and cross-sectional profile of the microchannels before and after filling. The single layer of printed ink resulted in a uniform filling of silver along the channel length, with thickness just under 1 µm, as measured by optical profilometry. However, as the number of layers increased to more than 1 layer, the ink started to overflow outside of the microchannel. This could be because these layers were printed with about 9 seconds of wait time between printing successive layers (9 seconds is the amount of time that it takes for the printhead to move to the home position and to return to the print position). This does not give enough time for the printed ink inside the microchannel to fully dry before the next layer of ink was printed. Furthermore, the total volume of the wet ink inside the microchannel was more than the volume of the microchannel and the ink started to overflow outside of the microchannel. The measured cross-sectional profile also confirms this overflow.

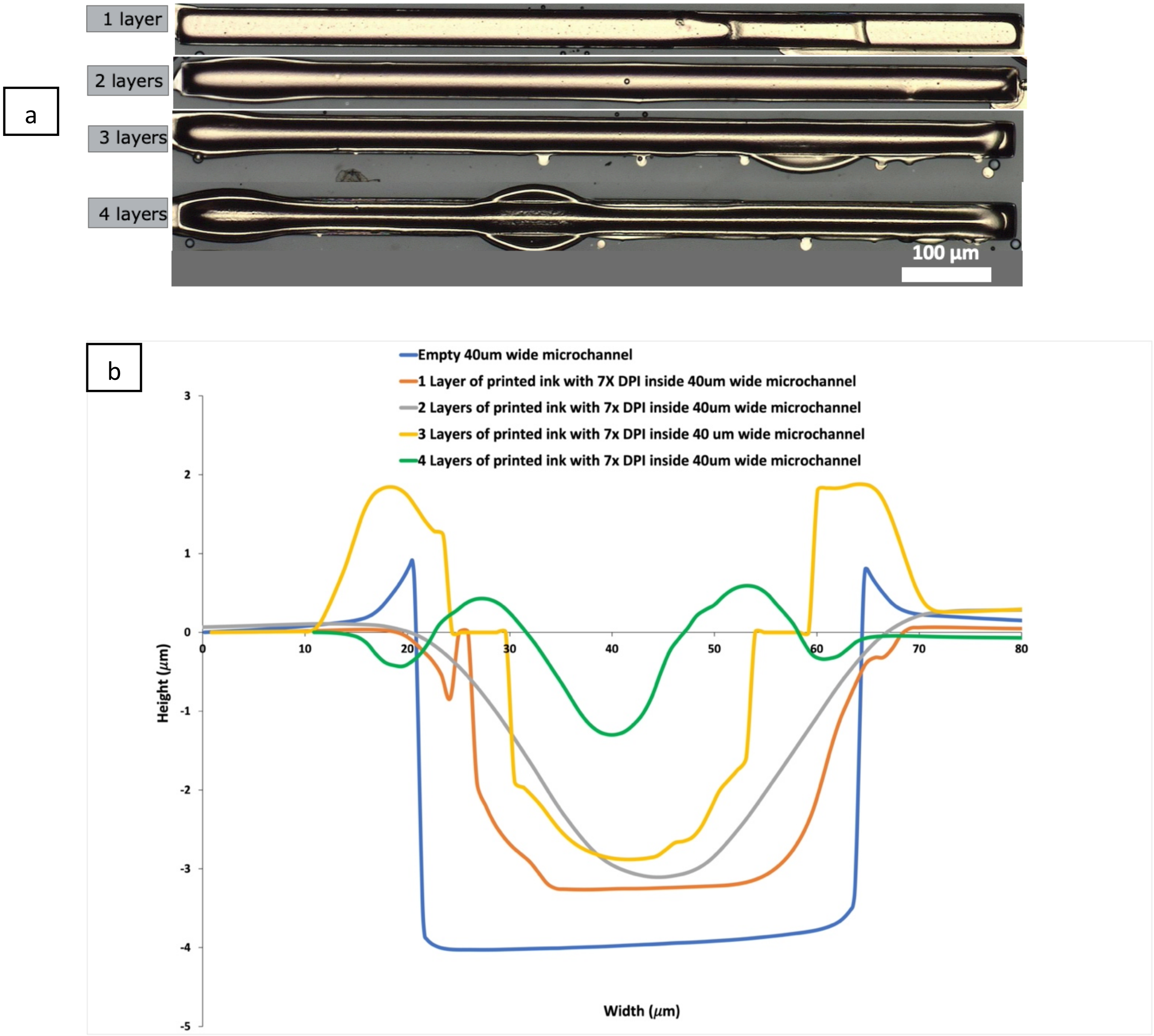

Figure 34. (a) Microscope image of microchannels created by UV-nanoimprint lithography in a photopolymer (Norland 85) on PET ST505 substrate filled with 1-4 layers of printed ink; (b) Plot of the cross-sectional profile of the microchannel before and after filling.

In order to make sure that each pass of the printed ink inside the microchannel was fully dry before the next layer was printed on top of it, two changes were made to our print setting parameters. First, the amount of ink that was printed inside the microchannel in each print pass was decreased by decreasing the DPI from 2520 (10 µm drop spacing) to 1080 (24 µm drop spacing) so that 2.3 times less ink was printed in each pass inside the microchannel. DPI could be further decreased, but the amount of time and number of passes that is needed to fill the microchannels also needs to be considered. The smaller DPI (larger drop spacing) we use, the more print passes we need to fill the microchannels, which will increase the amount of time that is needed to fill one microchannel. So, to compensate for the higher DPI that was chosen and to make sure that the printed layer was fully dry before the next layer was printed on top of it, another adjustment was made which was increasing the wait time between printing layers from 9 seconds to 6 minutes. To prevent the printhead nozzles from clogging during the longer wait time, ink was purged through the nozzles. Figure 35 shows the microscope image, and cross-sectional profiles of the microchannels filled with 5,10,15,20, and 25 layers with 1080 DPI (24 µm drop spacing) at 70 °C substrate temperature. The microscope image and cross-sectional profiles confirm that by decreasing the DPI and increasing wait time, we could successfully resolve the overflowing issue that we had for filling up microchannels with more than one layer of printed ink with 2520 (10 µm drop spacing). Here we show that by printing between 15 to 20 layers we should be able to fully fill the microchannels. The over-filling of the ink in the microchannels for layers between 15-20 layers can be helpful for the case of attaching surface mount electrical components to conductors filled in the microchannels.

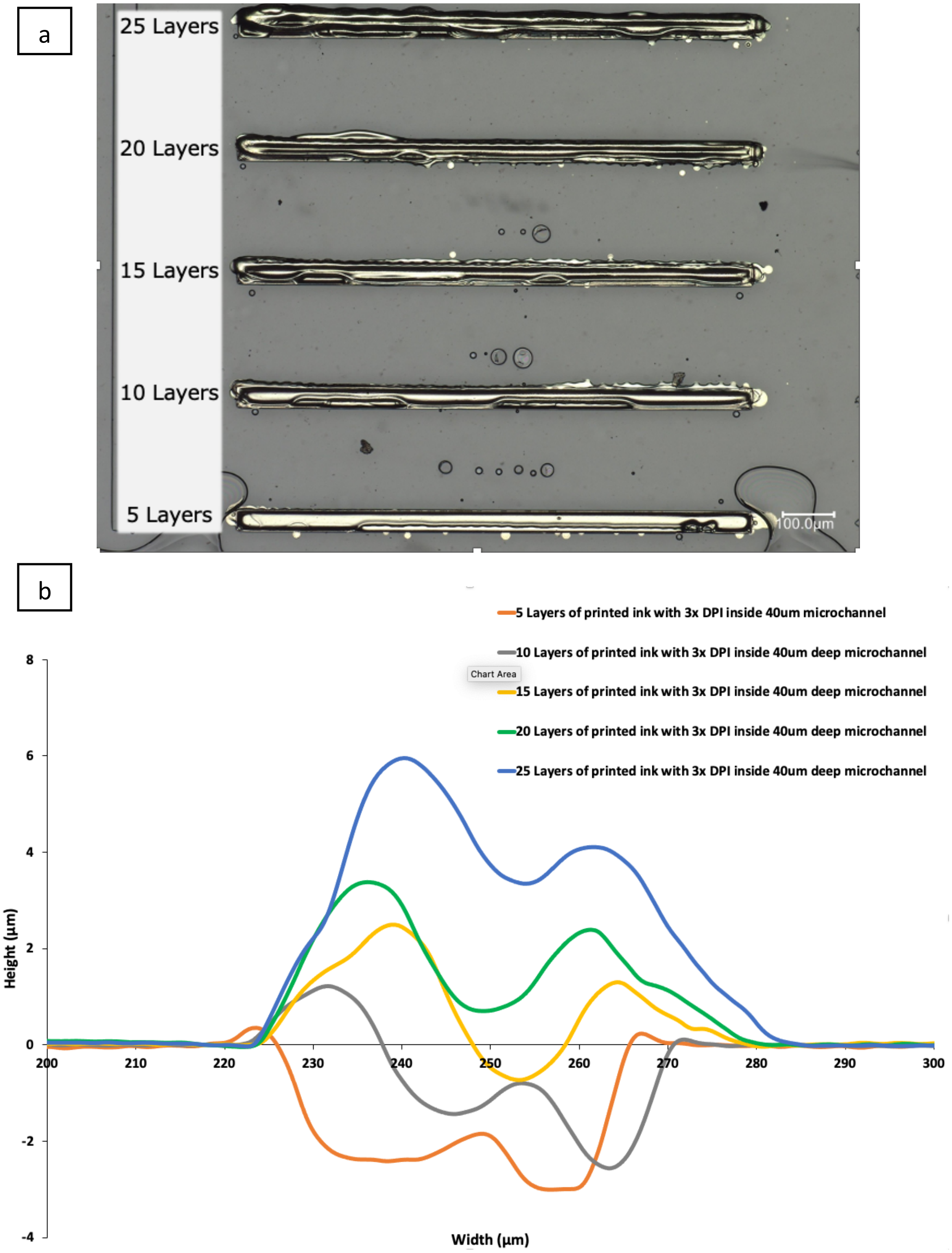

Figure 35. (a) Microscope image of microchannels created by UV-nanoimprint lithography in a photopolymer (Norland 85) on PET ST505 substrate filled with 5,10,15,20 and 25 layers of printed ink; (b) Plot of the cross-sectional profile of the microchannel after filling.

In order to improve our understanding of the role of microchannels on print resolution, we repeated the above-mentioned set of prints on PET ST505 with no microchannels. Figure 36 shows the microscope image, and line scans of 5,10,15,20, and 25 layers of 1pixel line printed on PET ST505 with 1080 DPI (24 µm drop spacing) at 70 °C substrate temperature. From the image and cross-section profiles, we can clearly see that for multiple layers of prints on PET ST505 (here we consider 15 layers as an example), the printed lines are about 218 µm in width, mainly due to the presence of spill over, while for 15 layers of printed lines on PET ST505, the width is between 40 to 50 µm. Spill over happens when the ink hits rough surface of previously printed and dried layer and splashing to the sides. For multiple layers of prints inside microchannels, we don't see spill over which we believe is due to the fact that the walls of the microchannel confine the ink and prevent it from flowing outwards and splashing. By comparing the height of the traces, we can also confirm that we could not reach more than 3µm in trace height for 15 layers of printed ink on PET ST505 while we could fill the 4µm deep microchannel and potentially have conductive traces with higher resolution, larger thickness, improved cross-section profile, and higher aspect ratio (thicker and narrower trace) which is desired because it will enable us to achieve high electrical conductance and small area footprint especially for traces that need to carry high current.

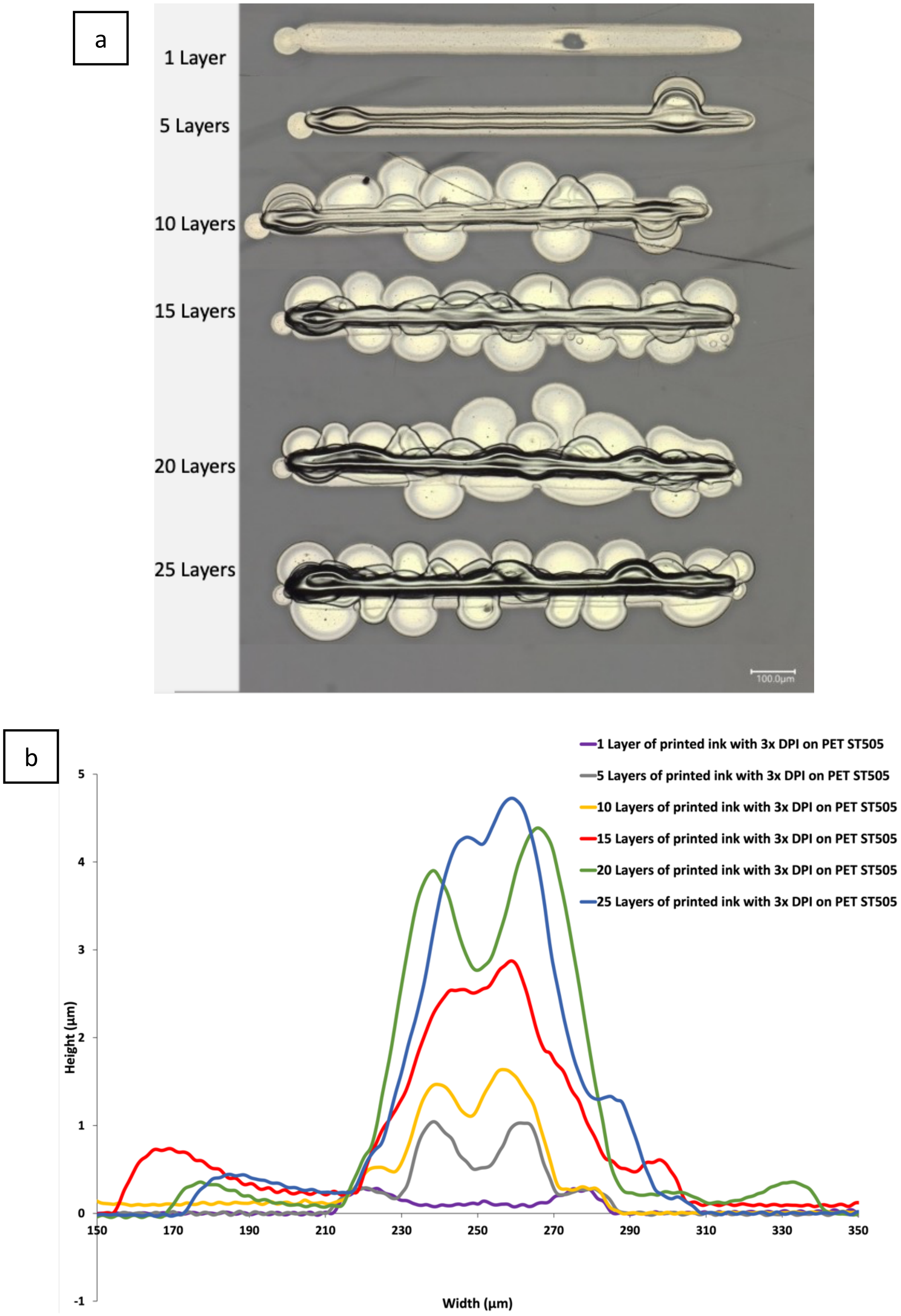

Figure 36. (a) Microscope image of 1,5,10,15,20 and 25 layers of printed ink on PET ST505 substrate (b) Plot of the cross-sectional profile of the prints.

As a suggestion for future work, since our study showed success in filling microchannels by printing along their whole length without relying on capillary effect, we believe that by further increasing the aspect ratio of the printed traces, inkjet printing can compete with other printing methods such as screen printing in printing traces with high aspect ratio and accordingly high electrical conductance.

5.5. Conclusions

Here we showed that by optimizing print parameters, we could successfully print into microchannels that are nominally 40 µm wide and ~4 µm deep at elevated temperature. We showed that we could print conductive traces with higher resolution, larger thickness, improved cross-section profile, and improved edge definition compared to stand-alone inkjet printing. This study proves that by printing inside microchannels we would be able to fill and even overfill channels with any length without relying on capillary-driven flow.

Chapter 6

Investigation of the effect of Surface Functionalization with Layer-by-layer Self-assembly on the interaction of ink and substrates

6.1. Introduction

Polyimide is a desirable substrate for inkjet printing of electronics because of its high temperature stability. However, the disadvantage is that inks that are not water-based (inks with low surface tension compared to that of water) spread out on the polyimide substrate due to low contact angles, leading to lower printing resolution (inability to print very narrow lines and small features). Polyimide substrates with fluorinated ethylene propylene (FEP) coating have much larger ink contact angles compared to that of the polyimide, which can enable high resolution printing. However, printing of narrow, continuous traces is limited to low substrate temperature (30 °C), which limits the rate of drying of the ink, and hence limits the throughput of printing. As shown in Figure 16, if the substrate temperature is increased to (70 °C) the ink balls up into discontinuous patches rather than forming a continuous trace. Furthermore, the adhesion of the printed materials to the substrate is very poor, which limits the practical applicability.

Surface functionalization is an effective way for controlling and enhancement of printability and adhesion of the inks to the substrates. Uniform coverage, predictable morphology and precisely controllable thickness makes self-limiting surface functionalization techniques such as Layer-by-Layer (LbL) an interesting candidate for surface engineering and coating industry. Layer-by-Layer (LbL) employs electrostatic self-assembly at the nanoscale. In this method, negatively (polyanionic) and positively charged (polycationic) polymer constituents are applied with a dip or spray in sequential layers and excess material is rinsed with de-ionized (DI) water and a composite will be formed due to the electrostatic attraction from their opposing charges. LbL coating characteristics can compete with vacuum-based self-limiting coating processes (such as Atomic Layer Deposition, ALD) for a wide range of applications. This method is now advanced from a batch-based process to a continuous multi-layer technology that is suitable for large-scale R2R manufacturing [36]

Here, using inkjet printing of DuPont PE410 silver nanoparticle ink, we demonstrate the application of two LbL coatings, Poly(Allylamine Hydrochloride) (PAH) and Branched Polyethylenimine (BPEI) onto FEP-coated polyimide substrates, Kapton FN. The work most relevant in this regard is by Fang et al [37]. They used LBL for modifying the surface of Kapton, polyimide, substrate and they showed that they could improve printability and adhesion of water-based and organic solvent-based inks on Kapton. However, as mentioned above, in order to enhance the printability and adhesion of inks with lower surface tension compared to that of water-based inks, and also in order to maintain high throughput printing, we study the LBL surface modification of Kapton FN and show that these coatings can achieve moderate ink contact angles in the 30-40° range and greatly improve the adhesion of the printed materials to the substrate. The moderate contact angles enable printing of continuous lines up to 70 °C, with much better print resolution (narrower linewidth and continuous lines) compared to on bare Kapton FN.

6.2. Objectives and Scope

As mentioned above, we hypothesize that two LBL coatings will enhance the printability of the ink on Kapton FN by resolving the balling up issue (shown in Figure 18) and will also enhance the adhesion of the ink to the substrate. To investigate these hypotheses, we have the following objective:

1. Study the effect of LBL coatings on printability of the ink on Kapton FN at elevated temperature through printing lines with various drop spacing and characterizing the printed lines using microscope imaging
2. Study the effect of LbL coatings on the adhesion of the ink to the substrate

6.3. Approach and Methods

In this study, we used Dupont PE410 silver conductive ink (Solvent-based, 45% Ag loading, 20-40 cP @ 25°C) as our conductive ink because of its high loading of silver nanoparticles and its compatibility with KM512-SH printhead. The substrates with LBL coatings were provided by Eastman Chemical Company. The substrate was first run through atmospheric corona plasma treater. After mounting the substrate onto glass carrier, aqueous polycation solution was sprayed uniformly onto the substrate and then the substrate was rinsed with DI water and was allowed to dry.

Advancing and receding contact angles were measured using Rame-Hart tensiometer/goniometer for 10 uL drop which is the smallest that can be easily produced using a pipette. The droplet was placed on the substrate, which was placed on sample stage, and then the stage was gradually tilted. Advancing contact angle was measured from the leading edge of the distorted droplet and the receding contact angle was measured from the trailing edge when the drop slides to move/slide [38]

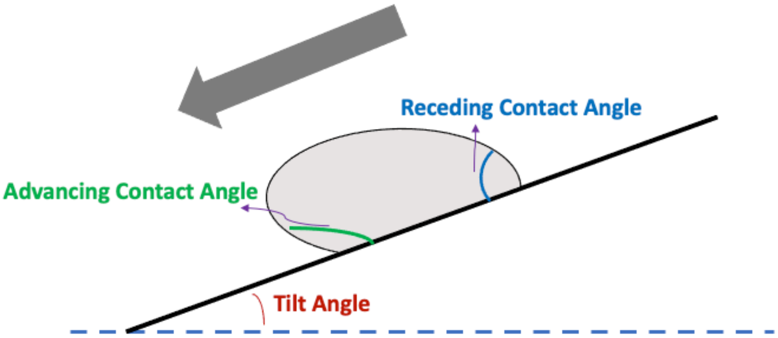

Figure 37. schematic of advancing and receding contact angle measurement using tilting method.

Keyence VHX-7000 microscope was used for imaging. Adhesion of the ink to the substrates was evaluated by printing a pad and annealing at 130 °C for 30 minutes in an oven, followed by performing a tape peel test per ASTM D3359. This involves first scoring crosshatched lines through the printed layer using a 6-blade tool, followed by applying and pressing down a standard tape using a pencil eraser, and then peeling it off at close to 180°.

6.4. Results and Discussion

6.4.1. Contact Angle of Ink

The measurement of advancing, receding and contact angle hysteresis for 10 µL drops of Dupont PE410 on Kapton FN, BPEI and PAH coated Kapton FN is shown in Figure 38. The measurement is the average of five separate measurements at separate locations. The advancing contact angle is the contact angle of the fluid when it advances, or the highest measurable contact angle, and the receding contact angle is the contact angle of the fluid when it recedes which is the lowest measurable contact angle [26]. Based on the contact angle measurements, for both Kapton FN and LbL coated Kapton FNs, the receding contact angle is not zero. With a non-zero receding contact angle, the ink can dewet the substrate and cause instability[19]; however, the LbL coatings are decreasing the receding contact angle and increasing the contact angle hysteresis.

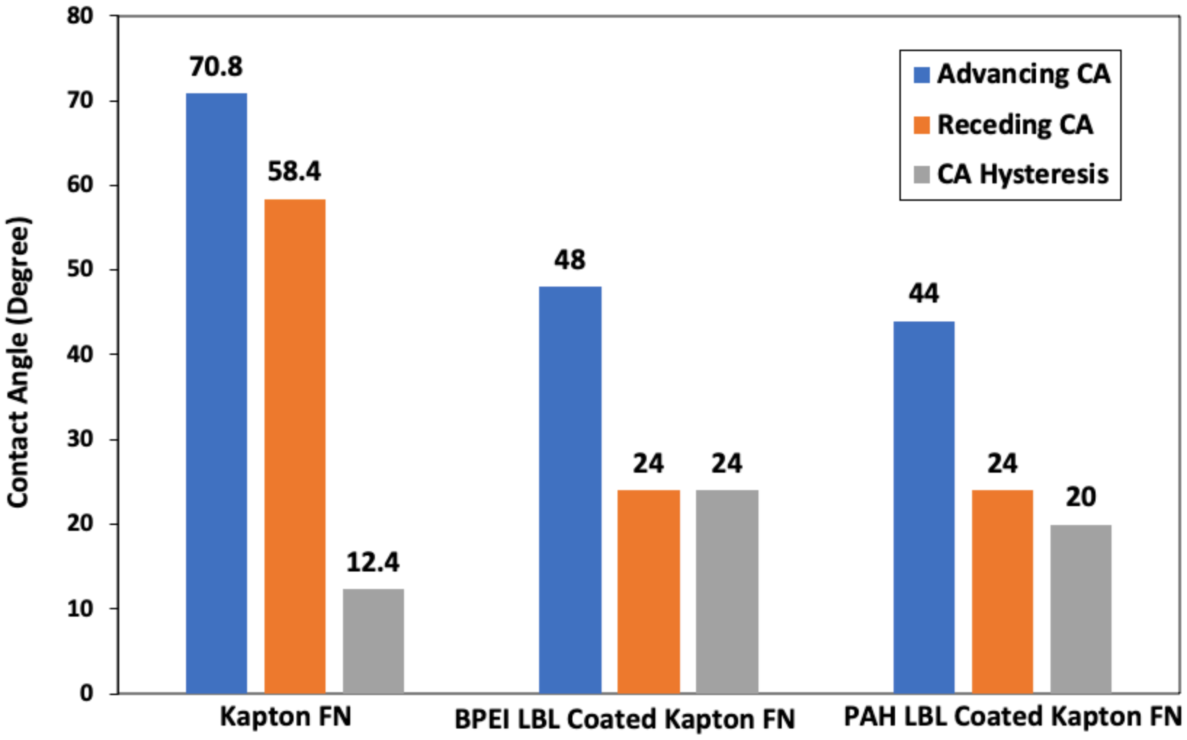

Figure 38. Advancing, receding and contact angle hysteresis for 10 µL drops of Dupont PE410 on Kapton FN, BPEI and PAH coated Kapton FN.

6.4.2. Prints on Kapton FN and LBL coated Kapton FN

1 pixel-wide traces on Kapton FN, and BPEI and PAH coated Kapton FNs were printed at 70°C substrate temperature. Drop spacings from 10 µm-60 µm with 5 µm increment were used for printing 1-pixel lines. The goal for changing the drop spacing was to investigate the effect of the LBL coatings on decreasing the receding contact angle, and consequently on the morphology of the printed lines. The range of drop spacings was narrowed down to 23 µm- 31 µm with 2 µm increment because it was found that for drop spacings of more than 31 µm, we just had individual drops, and with increasing the drop spacing, the drops just got further apart from one another and there was no change in the morphology of the printed drops. It was also found that for drop spacing of smaller than 23 µm, the bulging instability in the printed traces would become worse.

Accordingly, we narrowed down the range to 23-31 µm with smaller increment to investigate any little change in the morphology of the printed traces and to have a precise comparison between the lines printed on Kapton FN versus lines printed on Kapton FN with LbL coatings. Figures 39, 40, and 41 show the printed lines with selected drop spacings on Kapton FN, BPEI coated Kapton FN, and PAH coated Kapton FN, respectively.

Figure 39. 1 pixel-wide traces printed on Kapton FN with drop spacing from 23 µm to 31 µm.

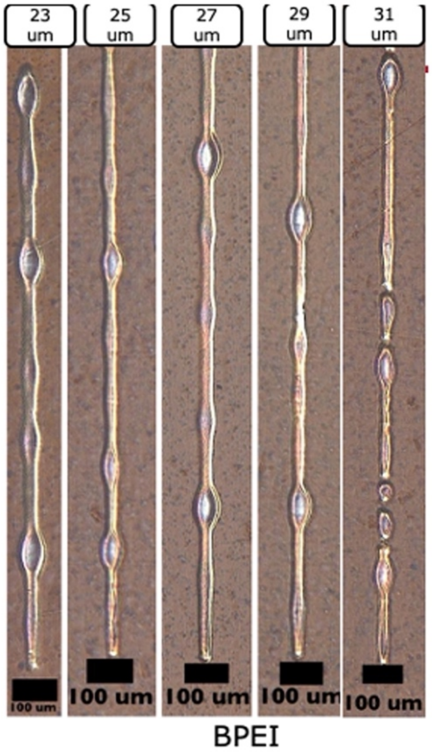

Figure 40. 1 pixel-wide traces printed on BPEI coated Kapton FN with drop spacing from 23 µm to 31 µm.

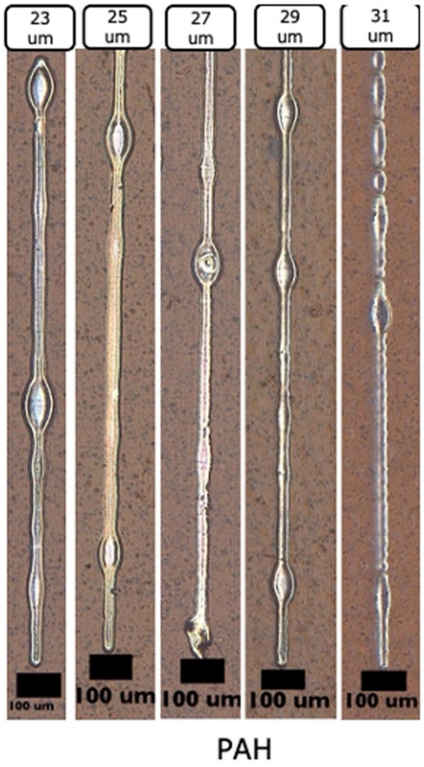

Figure 41. 1 pixel-wide traces printed on PAH coated Kapton FN with drop spacing from 23 µm to 31 µm.

Comparing Figures 39-41, for the 1 pixel-width lines printed on Kapton FN, BPEI coated Kapton FN, and PAH Coated Kapton FN, for drop spacings of 23 µm, 25 µm, and 27 µm, the lines are printed without any discontinuity because the LbL coatings decreased the receding contact angle and we believe the reason for enhancement in line continuity on LbL coated Kapton FNs compare to Kapton FN with no coating is this decrease in the receding contact angle. However, the traces still show bulging as a result of the receding contact angle not being zero.

Visual inspection of the LBL coated Kapton FNs revealed the fact that the LBL coatings are not uniform in all parts of the substrate, this non uniformity shows up as a wavy structure on the substrate which is shown in Figure 42.

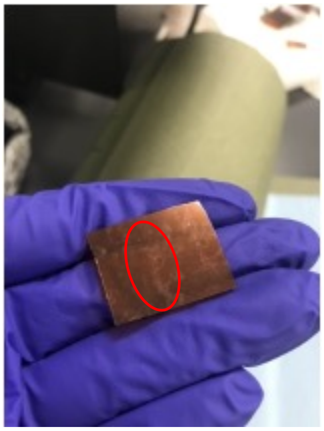

Figure 42. picture of non-uniformity of LBL coating on Kapton FN.

As a suggestion for future work, we believe that by resolving the non-uniformity issue of the LBL coatings and by increasing the number of layers of the coatings (in this research the substrates were only coated with one layer of the LBL coatings), the receding contact angle can be further decreased (closer to zero) which will lead to printing traces with enhanced resolution and less instability. To fully eliminate the bulging instability, the receding contact angle needs to be zero.

6.4.3. Adhesion of Dupont PE410 to Kapton FN and LbL coated Kapton FN

The adhesion of Dupont PE410 ink on Kapton FN with and without LbL coating was investigated by printing and annealing a pad. Curing was done by annealing once at 130 °C for 30 minutes in an oven and as mentioned before, the adhesion test was done by a tape peel test per ASTM D3359. Figure 43 shows the printed pad after the adhesion test was performed.

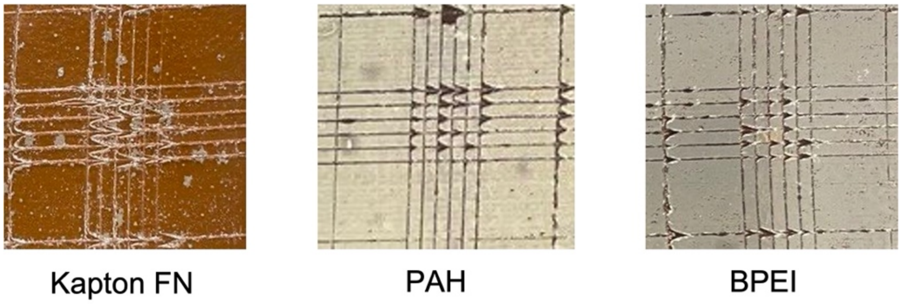

Figure 43. Printed pads after adhesion test.

Based on the adhesion test, it is shown that the adhesion of Dupont PE410 on Kapton FN is considerably enhanced after the substrates are coated with PAH and BPEI. The estimated ASTM adhesion rating for Dupont PE410 on Kapton FN coated with PAH and BPEI is 4B, and for Kapton FN is 0B. The decrease in contact angle hysteresis also confirms the fact that the adhesion is enhanced[39]

6.5. Conclusions

Layer-by-layer (LbL) coatings of PAH and BPEI was used to tune Kapton FN surface properties to enhance printability of continuous conductive traces with acceptable adhesion of the ink to the substrate at high temperature (70^{o}C) to allow high throughput of inkjet printing. Here, we showed that both LbL coatings decreased the receding contact angle of the ink Dupont PE410 and resolved the balling up issue of the ink at high temperature (70^{o}C) on Kapton FN. We also showed that Dupont PE410 does not adhere to Kapton FN and after coating the substrates with both LbL coatings, the adhesion of the ink to Kapton FN was enhanced considerably.

Chapter 7

Conclusions and Future Work

Our main goal in this research was to optimize the performance of inkjet printing using commercially available ink and substrates, focusing on print resolution to overcome one of the two main barriers that are currently preventing inkjet printing from being adopted for prototyping and volume manufacturing. By optimizing print settings, ink-substrate interaction, using a combination of NIL microfeature patterning with optimized geometry, and printing at elevated temperature, we could successfully print up to 2 layers of 33µm wide conductive traces, which is comparable with the best resolution that can be achieved by mature printing methods such as screen printing.

In another approach, we could successfully fill NIL microchannels that were nominally 40 µm wide and ~4 µm deep, and achieve conductive traces with higher resolution, larger thickness, improved cross-section profile, and improved edge definition compared to stand-alone inkjet printing. Our study shows that by printing inside microchannels we would be able to fill and even overfill channels with any length without relying on capillary-driven flow. This promising result can be adopted for printing inside deeper microchannels with higher aspect ratio closer to that of other printing methods, and accordingly achieving traces with higher conductivity.

We expect the success of the approaches that are used in this research for enhancing print resolution, can be adopted for other functional inks and dielectrics that are used in the manufacturing of FHE devices. We also expect that the results of this project can catalyze the adoption of inkjet printing of dielectric and other functional inks, and it can be used for optimizing the ink-underlayer interaction of multiple printing layers of conductors, dielectrics and encapsulants. Additionally, the surface modification of flexible substrates that were used in this research can be adopted for stretchable substrates that are used in wearable medical devices or sensor devices that are mounted on curved/stretchable surfaces. The electrical performance of stretchable traces that are present in wearable/stretchable sensors vary as it is bent or stretched so we suggest monitoring the resistance of these traces under repeated number of bending and stretching cycles. Overall, we believe that the results of this project can be used for opening up new FHE manufacturing opportunities.

The overall printed electronics market is estimated to reach $12.1B by 2022 and $73B by 2027 [40], so there is a need for manufacturing technologies that can seamlessly achieve both prototyping and volume manufacturing at low cost, to enable rapid development and commercialization of new FHE devices to support this growth. Optimized inkjet printing processes can facilitate this need so one of the main impacts of our project is economical. As mentioned in Chapter 1, one of the main applications of FHEs are sensing medical devices that can monitor vital signs such as pulse oxygenation, temperature, heart rate, respiration rate, and blood pressure. we expect that the success of research like ours in optimizing inkjet printing processes enable rapid development and commercialization of new FHE medical sensing devices. Accordingly, we believe the main social impact of our work to be protecting human health.

Chapter 8

Other Research Projects, Publications to Date and Planned Publications

During the course of my PhD, I worked on other research projects. One of the main projects that I worked on and resulted in a first-author paper is described here.

8.1. Controlling crystal growth of non-toxic Bismuth iodide (BiI3) semiconducting material for efficient photovoltaics

8.1.1. Introduction

During the past two decades, among unprecedented emergence of novel solar cells, perovskites and inorganic solar cells show the highest efficiencies with the potential to be less expensive, and flexible [41], [42]. However, among these solar cells, the best performing ones have lead (pb) as one of the elements in their absorber layers. Lead is among ten other elements which World Health Organization categorizes them as harmful for public health [43]. Therefore, there is a need for discovering non-toxic materials which have the potential to compete with best performing perovskite and inorganic solar cells.

Bismuth-based materials can be promising alternatives for materials which contain lead [44]. One of the promising candidates among bismuth-based materials is bismuth (III) iodide (BiI_3) due to its chemical similarity to Pb [45]. BiI_3 is a layered heavy metal semiconductor built from BiI_6 octahedra, with strong ionic bond of I-Bi and weak van der Waals interaction between planes, with promising anisotropic optical and electronic properties [46], [47]. BiI_3 have recently attracted researcher's attention as a promising material for PV application owing to its compelling properties. It has high absorption coefficient of 105 (cm^{-1}), and based on DFT calculations it has high electron mobility of 200 ± 50 ($cm^2V^1s^{-1}$) [48]. BiI_3 also have proper wide band gap of about 1.67 (ev), other band gaps also have been reported for BiI_3 up to about 2 (ev) which depends on the technique used to measure it [49].

There has been much research done on solution-processing BiI^3 for photovoltaics [46], [50], [51]. In the solution-processing of BiI_3, the BiI_3 powder is dissolved either in dimethylformamide (DMF) [50]–[52] or tetrahydrofuran (THF) [46], [50] since it is highly soluble in both solvents [50]. Then, the solution is spin coated on the substrate. It is found that annealing in solvent vapor reduces film porosity, increases grain size and improves carrier mobility which results in enhancement of performance of the device [50]. Hamdeh et al. reported the highest efficiency resulting from solution processing of their BiI_3 film following by solvent vapor annealing [50]. Tiwari et al. reported synthesizing BiI_3 film by first spin coating $Bi(NO_3)_3$ and thiourea precursor solution following by a thermolysis step to make a Bi_2S_3 film, and then annealing the film upon exposure to I_2 gas to make BiI_3 film. They reported a record open circuit voltage of 600(mV) and they attribute this high open circuit voltage to the good quality of their BiI_3 film [53]. Physical vapor deposition/transport is another method which can be used for the synthesis of BiI_3 thin films. Comparing to solution-processing, few research has been conducted so far on this synthesis method. Brandt et al. were the first researchers who used physical vapor transport method for the synthesis of BiI_3 film on quartz. They investigated the challenges and potentials of using BiI_3 for PV application [54]. Zhu et al. used vapor-solid-solid reaction for synthesizing stable vertically aligned BiI_3 nanosheets. First, they thermally evaporated the bismuth precursor, and then they annealed their samples in iodine vapor which lead to the growth of their BiI_3 films. They showed that having a 3D vertically aligned nanosheets enhanced the light absorption and carrier collection in their solar cell and they could achieve a record power efficiency of 1.45% [47]. Compared to solution-processing of BiI_3 film, physical vapor deposition (PVD) has not been studied much as a facile way of synthesizing BiI_3 films.

It is difficult to achieve both high light absorption and photo carrier collection especially in solar cell with polycrystalline structure with crystals which are randomly oriented, that is why there is a need for controlling the crystal structure of the absorber layer. Based on simulation studies, 3D structures such as vertical arrays enhance the photocarrier separation and collection by orthogonalizing the direction of light absorption and photo carrier separation [55]–[57]. Here, we developed a custom-built PVD system, close space sublimation (CSS), and controlled the crystal growth of BiI_3 thin film. We directly sublimed BiI_3 powders in a ones step process which is a transfer-free and easy yet unique method. Also, by controlling the CSS parameters, we could successfully control the orientation of the crystals. We achieved a record of 0.6(ns) for photoexcited carrier lifetime that is higher than the ones previously reported in experimental studies [47], [54] which shows enhanced photo carrier collection and separation in our crystals. The optimized vertical BiI_3 nanoflake device showed a power conversion efficiency of 0.6%. Higher efficiencies can be obtained by optimizing the band alignment between TiO_2 as electron transport layer, BiI_3 as the absorber, and F_8 as hole transport layer, and by further optimizing the transport layers. Throughout this work, we paved the way for controlling the orientation and morphology of BiI_3 for efficient solar cells by using a facile, and scalable method.

8.1.2. Approach and Methods

Synthesis: BiI_3 powder (Sigma Aldrich, 99%) was used for making BiI_3 thin films. A custom-built close space sublimation (CSS) system (Figure 44) was used to grow BiI_3 nanoflakes and nanocrystals directly on FTO-coated glass substrates. The system consists of a 2 in. diameter quartz tube that enclosed a stainless steel (SS) fixture for holding the FTO substrate, and a custom-made stainless-steel source boat (L × W × H = 25 mm × 7 mm × 5 mm) containing BiI_3 powder. A rotary vane pump (KJLC-RV206) was used to pump down the tube. A heat wrap (manufactured by BriskHeat) was used to provide heat externally. The substrate temperature was controlled by the flow rate of water through the substrate holder. Source and substrate temperatures were measured using thermocouples that were in contact with the source and substrate. For the growth, FTO substrate was mounted upside down towards the source boat onto the underside of the water-cooled substrate holder using stainless steel wires. The tube was pumped down to about 200mTorr and then heated by the heating wrap. After the desired deposition time had elapsed, the heating system was stopped, and the system was allowed to cool naturally to room temperature. The quartz tube was vented, and the sample was removed.

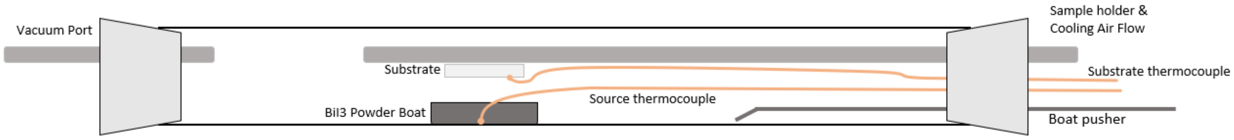

Figure 44. Schematic drawing of CSS system.

Electron transport layer, hole transport layer and contacts: FTO glass (Hartford Glass, IN) substrates of typical size 2 cm × 2.5 cm were sonicated and cleaned three times in a 1:1:1 mixture of isopropanol, acetone, and deionized water. Then they were dried with compressed air. Compact-TiO_2 (c-TiO_2) was used as the electron transport layer (ETL). A solution of 0.055ml Titanium di(isopropoxide) bis(2,4-pentanedionate) (75% in propanol, Alfa Aesar) in 1ml of 1-butanol (anhydrous, 99.8%, Sigma Aldrich) was spin coated on the cleaned FTO at 2000rpm for 30 seconds following by annealing on hot plate at 125^{o}C for 5min. Then, a solution of 0.11ml Titanium di(isopropoxide) bis(2,4-pentanedionate) (75% in propanol) in 1ml of 1-butanol was spin coated two times at 2000rpm for 30 seconds following by annealing on hot plate at 125 ^{o}C for 5min. As the last step in making the ETL, the sample was thermally annealed at 500°C for 30 min. Poly (9,9-di-n- octylfluorenyl-2,7-diyl) (PFO, Sigma Aldrich) was used as the hole transport layer. 10mg of PFO was dissolved in 1ml of chlorobenzene (anhydrous, 99.8% Sigma Aldrich) and then spin coated at 2000rpm for 30 seconds. For the top contact gold (Au) was thermally evaporated. Finally, the whole cell was annealed at 100°C for 10 minutes.

Characterization Methods: The morphologies and crystal structures of nanostructured BiI_3 were characterized using SEM (JEOL 7000F, 10 kV), and parallel beam XRD (PANalytical Empyrean, Cu kα, 45 kV, 40 mA). The photoluminescence (PL) of BiI_3 was measured using a Horiba iHR550 spectrometer with 532 nm fiber-coupled laser and a Horiba Synapse CCD camera. Time-resolved photoluminescence (TRPL) was measured at room temperature using Becker and Hickl's time-correlated single photon counting system (SPC-150) and ID Quantique's single photon avalanche photodiode (ID-100-50-STD). The pump was a 20 ps pulsed laser with a frequency of 19.4 MHz, average power of 0.5 μW, and a spot size of about 1 mm^2. Accordingly, the instantaneous peak intensity of the pulsed laser incident on the sample was about 128 mW cm^2, which was similar to 1 sun condition.

The power conversion efficiency (PCE) of devices was determined using current-voltage (J-V) curves under solar simulation. The simulated sunlight for these measurements was provided by a xenon lamp (model 6258, Oriel) equipped with an AM 1.5G filter (model 81094, Oriel).

8.1.3. Results and Discussion

8.1.3.1. Controlling Crystal Growth

As our first goal, we tried to control the crystal orientation of the BiI_3 thin films. As mentioned in the section 7.1.2, our CSS system was designed in a way to control the source and substrate temperature independently. Controlled experiments were designed to investigate the effect of the difference between source and substrate temperature (ΔT) on the orientation of the grown crystals. The source temperature was controlled in the range of 180°C-230°C, the substrate temperature was controlled in the range of 125°C-180°C, and the growth duration was fixed at 10min. Scanning electron microscopy (SEM) was carried out to characterize the morphology.

From Figure 45, it is clear that for ΔT lower than 50°C, the crystal growth is favoring horizontal growth while at ΔT higher than 70°C, the crystal growth is favoring vertical growth. It can be also observed that as the crystal orientation is transitioning from horizontal to vertical crystals by increasing the ΔT, the surface coverage is becoming more, and we have a dense and uniform thin film. The nucleation of BiI_3 is driven by the negative free energy change of vapor to solid condensation of BiI_3 from super saturated vapor (ΔGSV). On the other hand, the entropy change of condensation of vapor is also negative, so by reducing the substrate temperature, ΔGSV becomes more negative and larger in magnitude which leads to higher nucleation rate. Also, by decreasing the substrate temperature, the growth rate decreases and makes it easier for nuclei to form for longer time. Accordingly, at lower substrate temperatures (higher ΔT, higher supersaturation), the nucleation rate is more, and we have higher density of vertical crystals (nanoflakes). At higher substrate temperatures (lower ΔT, lower supersaturation), the nucleation rate is less, and there is enough energy for BiI_3 molecules to diffuse and nucleate from a previously grown 2D horizontal crystal instead of forming a new flat horizontal interface with the substrate. That is why in horizontal crystals, we have thicker crystals with less density (more empty space in between them) [58], [59].

As mentioned above, horizontal BiI_3 crystals are not as uniform as vertical films of BiI_3 nanoflakes and have poor coverage. Poor coverage increases the chance of short circuit happening in cells and running the efficiency. That is why for our goal of making solar cells out of the deposited films, we tried to optimize the synthesis parameters of vertically grown nanoflakes (ΔT > 90°C).

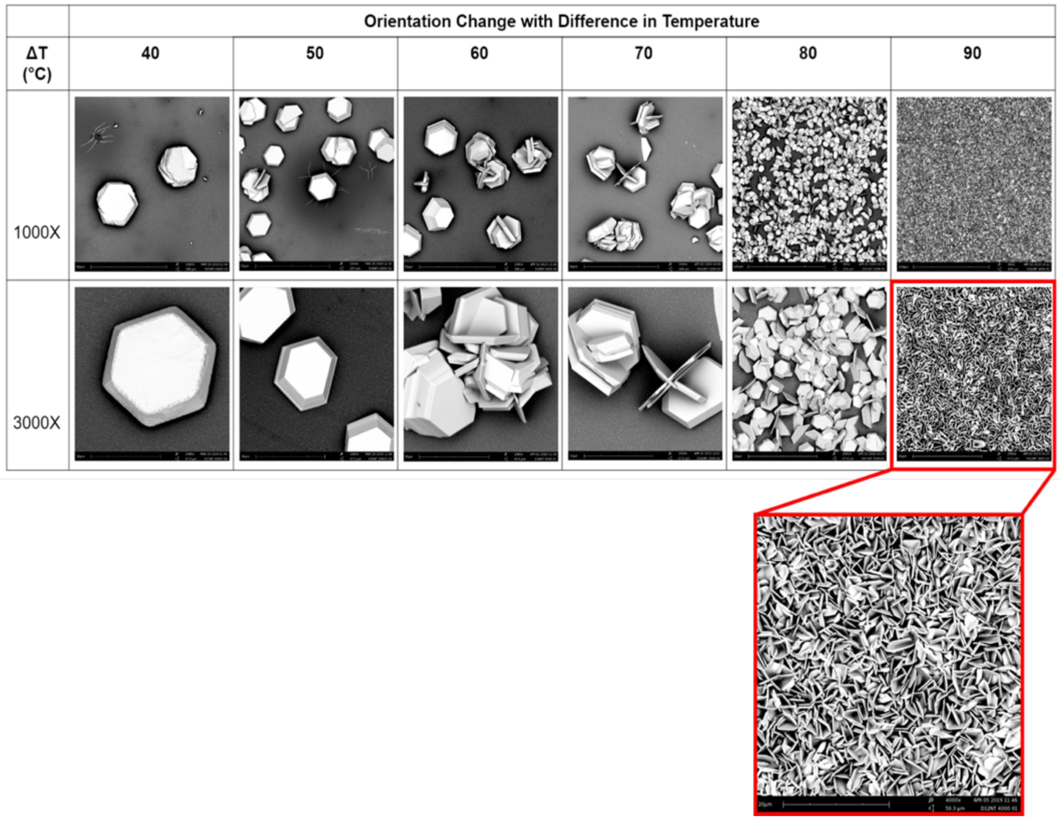

Figure 45. Crystal orientation change with change in ΔT.

8.1.3.2. Optimization of Growth of Vertical BiI_3 Nanoflakes

According to the SEM images shown in section 7.1.3.1, for ΔT > 90°C, we could successfully grow vertical nanoflakes. For the optimization of parameters, ΔT was fixed at 100°C to ensure uniform vertical growth of the nanoflakes. To confirm the crystal structure of the nanoflakes, the XRD pattern of as-grown BiI_3 nanoflakes was characterized (Figure 46). The XRD pattern matches well with the mixed peaks of the FTO and BiI_3. The XRD pattern of the grown sample shows the peak from (300) plane which confirms that nanoflakes are vertically grown.

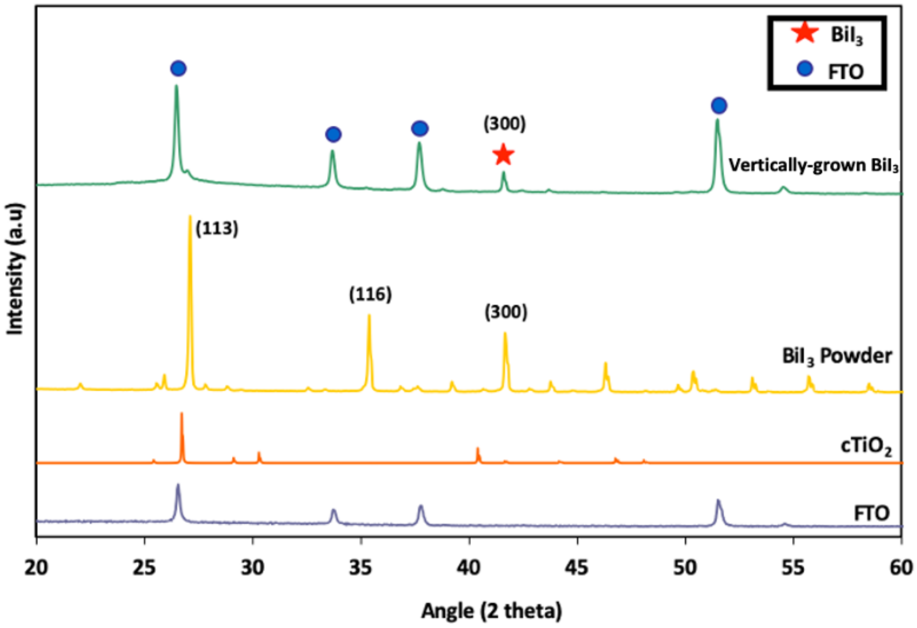

Figure 46. X-ray diffraction patterns of bare FTO, FTO/cTiO$_2$, and FTO/cTiO$_2$/BiI$_3$

Substrate temperature was chosen between 80ºC-120ºC. Increasing substrate temperature higher than 100ºC resulted in the visible degradation of BiI$_3$ film, the film became lighter in color. Accordingly, to make sure the thin film is not degrading and remains uniform, we kept substrate temperature fixed at 80ºC. To optimize the growth duration, by keeping ΔT at 100ºC and Substrate temperature at 80ºC fixed, we tried growth duration of 5min, 10min, 15min, and 20min. Growth parameters are shown in table 10.

Samples	**Substrate temperature**	**Source temperature**	**ΔT**
5min	80ºC	180ºC	100ºC
10min	80ºC	180ºC	100ºC
15min	80ºC	180ºC	100ºC
20min	80ºC	180ºC	100ºC

Table 10. Growth parameters of vertical nanoflakes.

Figure 47 shows the cell performance of samples 5min, 10min, 15min, and 20min. By increasing the growth time, the J_{sc} increases and reaches the maximum amount of 3.5 mA/cm^2 for 15min sample, and for 20min sample it decreases. The change in V_{oc} is not consistent which shows some potential problem with transport layers uniformity, and probable lack of coverage, however the V_{oc} of 15min sample is the maximum amount of 280 mV. In sum, The V_{oc} and J_{sc} of 15min sample are the highest amounts which shows that optimized time for growth is 15min. Owing to the fact that the film thickness plays a key role in charge transport mechanism in thin films [60], we predict that by increasing growth duration up to 20min and subsequent increase in film thickness, charge transfer is negatively affecting V_{oc} and J_{sc} of 20min sample. So, in this work we could successfully optimize the thickness of BiI_3 layer, but optimization of transport layers is required.

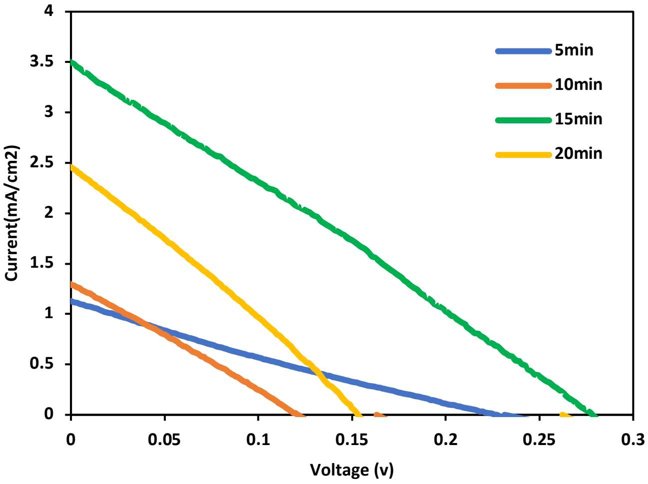

Figure 47. J-V curve of vertically grown nanoflakes.

Figure 48 shows the SEM images of the top and cross section of 15min samples. Based on the cross-section image, the optimized thickness of the physically deposited BiI_3 nanoflakes for charge transfer is about 500nm.

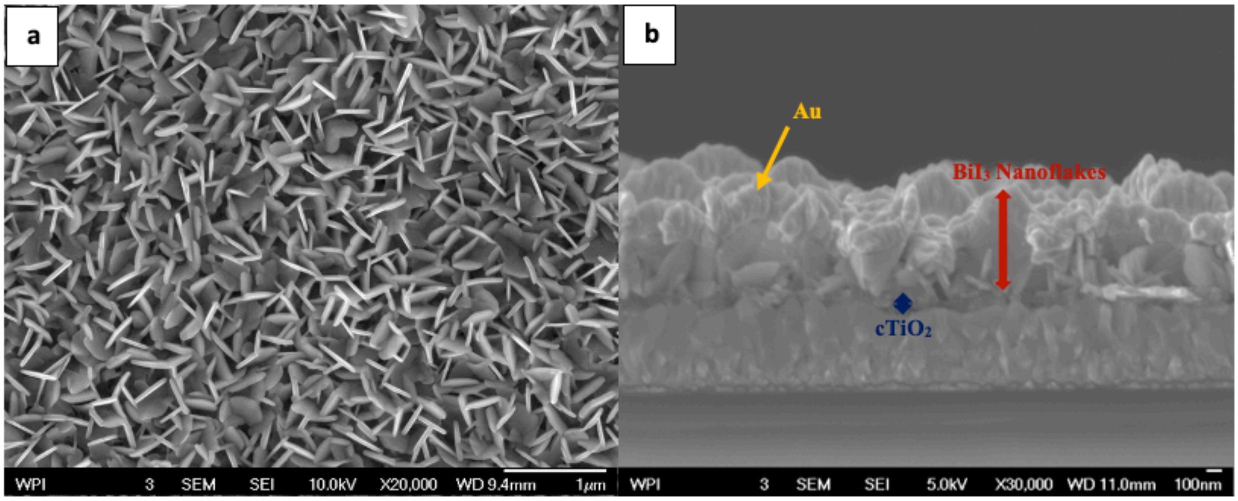

Figure 48. SEM image of (a) Top view of 15min optimized sample, (b) cross-section view of full cell including the ETL, absorber, and contact.

We performed photoluminescence (PL) using a pump wavelength of 532nm. As shown in Figure 49a, the PL peak center at 1.82 (ev) which is in agreement with the band gap of BiI_3 [50], [54], [60]. Time resolved photoluminescence (TRPL) was used for characterizing the radiative lifetime of photoexcited carriers in BiI_3. We used a 405 nm wavelength laser to excite the optimized BiI_3 sample (figure 46b). Immediately after the excitation, a fast response with a lifetime of about 83 (ps) is observed, which is attributed to the response of the measurement system. After fitting a double exponential, the radiative carrier lifetime in BiI_3 nanoflakes is estimated to be ≈0.6 ns which is the highest radiative lifetime of carriers reported among experimental studies [47], [54].

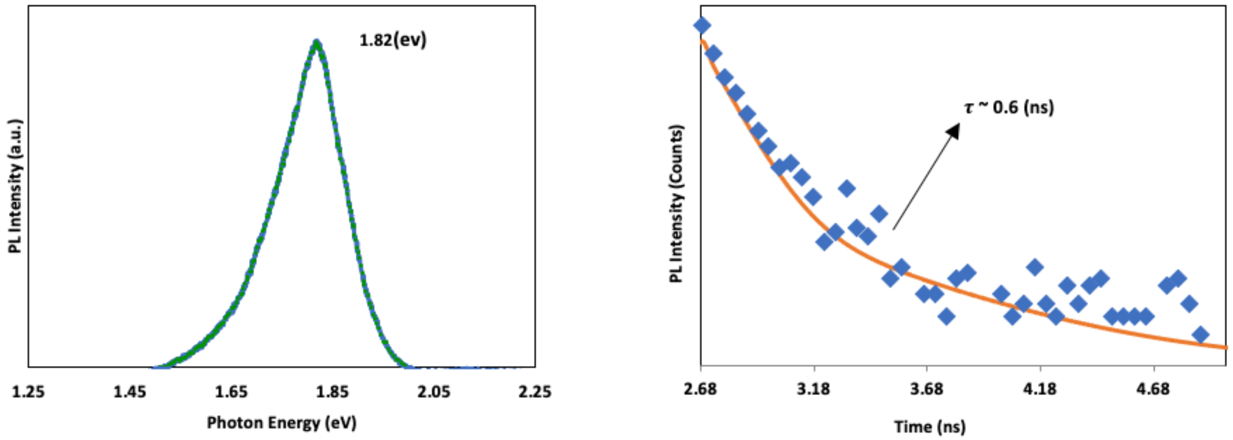

Figure 49(a) Steady-state photoluminescence spectrum, (b) Time-resolved photoluminescence of vertical BiI_3 nanoflakes following photoexcitation with 405 nm, ≈20 (ps) pulses.

8.1.4. Conclusions

In summary, we have designed a unique close space sublimation system, and successfully controlled and optimized the crystal growth of BiI_3 crystals on FTO substrate by controlling the source temperature, substrate temperature, and growth duration. We have shown that by having a difference between the source and substrate temperature higher than 90°C, the crystals tend to grow vertically, and they form a uniform film compared to that of horizontal BiI_3 crystals which is ideal for PV application. The optimized vertical nanoflakes exhibit photoexcited carrier lifetime of 0.6 ns which is the highest one reported so far and exhibits the enhanced charge collection and separation in the optimized sample. The optimized BiI_3 film exhibit a suitable band gap of 1.8 (ev) which is in agreement with other reports. The device built from the optimized nanoflake show Isc~3.5 mA/cm^2, and V_{oc} of about 280 mV. We attribute the low J_{sc} and V_{oc} of the optimized BiI_3 nanoflake to the unfavorable band alignment between TiO_2 as electron transport layer, BiI_3 as the absorber, and PFO as hole transport layer. With our work, we present a unique, and scalable method for the synthesis of not only BiI_3 2D crystals, but also other layered materials with providing the capability of having control over morphology and crystal growth.

8.2. Publications To Date

1. Rao PM, Pratt N, **Masroor M,** Influence of process parameters on inkjet printing of silver conductive traces for digital additive manufacturing of flexible electronics, IPC Apex Expo, 2022.

2. **Masroor M**, Yan T, McRae J, Molstad E, Rivas R, Ruano E, McClelland A, Rao PM. Controlling crystal growth of non-toxic Bismuth iodide (BiI3) semiconducting material for efficient photovoltaics. InPhysics, Simulation, and Photonic Engineering of Photovoltaic Devices IX 2020 Mar 3 (Vol. 11275, p. 112750H). International Society for Optics and Photonics.

3. Giri B, **Masroor M**, Yan T, Kushnir K, Carl AD, Doiron C, Zhang H, Zhao Y, McClelland A, Tompsett GA, Wang D. Balancing light absorption and charge transport in vertical SnS2 nanoflake photoanodes with stepped layers and large intrinsic mobility. Advanced Energy Materials. 2019 Aug;9(31):1901236.

4. Zhou L, Bainglass E, **Masroor M**, Giri B, Li G, Carl A, Grimm RL, Huda MN, Titova LV, Rao PM. Synthesis and optoelectronic properties of a promising quaternary metal oxide light absorber CuBiW 2 O 8. Journal of Materials Chemistry A. 2021;9(3):1643-54.

5. Mughal MA, Alqudsi A, Rao PM, **Masroor M**, Ichwani R, Zhou L, Giri B. All-electrodeposited p-Cu 2 ZnSnS 4/n-In 2 S 3 Heterojunction Formation for Solar Cell Applications. In2018 IEEE 7th World Conference on Photovoltaic Energy Conversion (WCPEC)(A Joint Conference of 45th IEEE PVSC, 28th PVSEC & 34th EU PVSEC) 2018 Jun 10 (pp. 0142-0147). IEEE.

8.3. Planned Publications

1. Surface with Microfeature Array and Method for Printing of Ink on the Surface for Improved Resolution, Edge Definition, Dimensional Tolerance and Adhesion, **Maryam Masroor**, Pratap M. Rao, John Berg, Tentative, 2022

2. Surface with Microchannels and Method for Printing of Ink into Microchannels, **Maryam Masroor**, Pratap M. Rao, John Berg, Tentative, 2022

3. Improvement of Inkjet Print Resolution and Adhesion of Silver Nanoparticle Inks on Polyimide Substrates by Application of Layer-by-Layer Coatings, **Maryam Masroor**, Pratap M. Rao, Chris Stoessel, Tentative, 2022

4. Using High Substrate Temperature for Enhancing Print Resolution: Understanding the Role of Drying, **Maryam Masroor, Nicholas Pratt (Joint First Author)**, Pratap M. Rao, Tentative, 2022.

References

[1] A. C. Arias, J. D. MacKenzie, I. McCulloch, J. Rivnay, and A. Salleo, “Materials and applications for large area electronics: Solution-based approaches,” *Chemical Reviews*, vol. 110, no. 1, pp. 3–24, Jan. 2010, doi: 10.1021/cr900150b.

[2] N. Palavesam, S. Marin, D. Hemmetzberger, C. Landesberger, K. Bock, and C. Kutter, “Roll-to-roll processing of film substrates for hybrid integrated flexible electronics,” *Flexible and Printed Electronics*, vol. 3, no. 1, Mar. 2018, doi: 10.1088/2058-8585/aaaa04.

[3] Y. Khan, A. Thielens, S. Muin, J. Ting, C. Baumbauer, and A. C. Arias, “A New Frontier of Printed Electronics: Flexible Hybrid Electronics,” *Advanced Materials*, vol. 32, no. 15. Wiley-VCH Verlag, Apr. 01, 2020. doi: 10.1002/adma.201905279.

[4] “https://www.nextflex.us/.”

[5] S. M. F. Cruz, L. A. Rocha, and J. C. Viana, “Printing technologies on flexible substrates for printed electronics,” in *Flexible electronics*, IntechOpen, 2018.

[6] G. Grau, J. Cen, H. Kang, R. Kitsomboonloha, W. J. Scheideler, and V. Subramanian, “Gravure-printed electronics: recent progress in tooling development, understanding of printing physics, and realization of printed devices,” *Flexible and Printed Electronics*, vol. 1, no. 2, p. 023002, 2016.

[7] N. J. Wilkinson, M. A. A. Smith, R. W. Kay, and R. A. Harris, “A review of aerosol jet printing—a non-traditional hybrid process for micro-manufacturing,” *The International Journal of Advanced Manufacturing Technology*, vol. 105, no. 11, pp. 4599–4619, 2019.

[8] Y. Khan, A. E. Ostfeld, C. M. Lochner, A. Pierre, and A. C. Arias, “Monitoring of vital signs with flexible and wearable medical devices,” *Advanced materials*, vol. 28, no. 22, pp. 4373–4395, 2016.

[9] C.-W. Lee, D.-H. Nam, Y.-S. Han, K.-C. Chung, and M.-S. Gong, “Humidity sensors fabricated with polyelectrolyte membrane using an ink-jet printing technique and their electrical properties,” *Sensors and Actuators B: Chemical*, vol. 109, no. 2, pp. 334–340, 2005.

[10] P. Escobedo *et al.*, “Flexible passive near field communication tag for multigas sensing,” *Anal Chem*, vol. 89, no. 3, pp. 1697–1703, 2017.

[11] “Optomec. (2018). Aerosol Jet - Printed Antennas.,” *Available: https://www.optomec.com/printed- electronics/aerosol-jet-core-applications/printed-antennas/.*

[12] L. Nayak, S. Mohanty, S. K. Nayak, and A. Ramadoss, “A review on inkjet printing of nanoparticle inks for flexible electronics,” *Journal of Materials Chemistry C*, vol. 7, no. 29, pp. 8771–8795, 2019, doi: 10.1039/c9tc01630a.

[13] J.E. Fromm, “Numerical Calculation of the Fluid Dynamics of Drop-on-Demand Jets,” *IBM Journal of Research and Development*, 1984.

[14] N. Reis and B. Derby, “Ink Jet Deposition of Ceramic Suspensions: Modeling and Experiments of Droplet Formation,” *MRS Proceedings*, vol. 625, p. 117, Feb. 2000, doi: 10.1557/PROC-625-117.

[15] de K. M. B. M. S. A. M. K. et al. Duineveld PC, “Ink-Jet Printing of Polymer light-emitting devices.”

[16] Stow C. D. and Hadfield M. G., “An experimental investigation of fluid flow resulting from the impact of a water drop with an unyielding dry surface,” *Proc. R. Soc. Lond. A373419–441*, 1981.

[17] B. Derby, “Inkjet printing of functional and structural materials: Fluid property requirements, feature stability, and resolution,” *Annual Review of Materials Research*, vol. 40, pp. 395–414, 2010, doi: 10.1146/annurev-matsci-070909-104502.

[18] B. Derby and N. Reis, “Inkjet Printing of Highly Loaded Particulate Suspensions,” *MRS Bulletin*, vol. 28, no. 11, pp. 815–818, Nov. 2003, doi: 10.1557/mrs2003.230.

[19] P. C. Duineveld, “The stability of ink-jet printed lines of liquid with zero receding contact angle on a homogeneous substrate,” *Journal of Fluid Mechanics*, no. 477, pp. 175–200, Feb. 2003, doi: 10.1017/S0022112002003117.

[20] P. J. Smith, D.-Y. Shin, J. E. Stringer, B. Derby, and N. Reis, “Direct ink-jet printing and low temperature conversion of conductive silver patterns,” *Journal of Materials Science*, vol. 41, no. 13, pp. 4153–4158, 2006, doi: 10.1007/s10853-006-6653-1.

[21] J. C. A. F. Bashforth, *An Attempt to Test the Theories of Capillary Action: By Comparing the Theoretical and Measured Forms of Drops of Fluid*, vol. University Press. 1883.

[22] J. D. Berry, M. J. Neeson, R. R. Dagastine, D. Y. C. Chan, and R. F. Tabor, “Measurement of surface and interfacial tension using pendant drop tensiometry,” *Journal of Colloid and Interface Science*, vol. 454, pp. 226–237, 2015, doi: https://doi.org/10.1016/j.jcis.2015.05.012.

[23] S. Schmieschek and J. Harting, “Contact angle determination in multicomponent lattice Boltzmann simulations,” *Communications in Computational Physics*, vol. 9, no. 5, pp. 1165–1178, 2011, doi: 10.4208/cicp.201009.271010s.

[24] H.-S. H. Y.-C. K. J.-P. A. M.-R. O. K. E. L. J.-W. L. P.-R. C. H.-K. S. & H. J. Jimin Park, “Direct and accurate measurement of size dependent wetting behaviors for sessile water droplets,” *Scientific Reports*, 2015.

[25] D. Soltman and V. Subramanian, “Inkjet-printed line morphologies and temperature control of the coffee ring effect,” *Langmuir*, vol. 24, no. 5, pp. 2224–2231, 2008.

[26] A. Marmur, “Thermodynamic aspects of contact angle hysteresis,” *Advances in Colloid and Interface Science*, vol. 50, pp. 121–141, 1994, doi: https://doi.org/10.1016/0001-8686(94)80028-6.

[27] H. SIRRINGHAUST. KAWASER. H. FRIENDT. SHIMODAM. INBASEKARANW. WUAND E. P. WOO, “High-Resolution Inkjet Printing of All-Polymer Transistor Circuits,” *Science (1979)*, 2000.

[28] C. W. Sele, T. von Werne, R. H. Friend, and H. Sirringhaus, “Lithography-free, self-aligned inkjet printing with sub-hundred-nanometer resolution,” *Advanced Materials*, vol. 17, no. 8, pp. 997–1001, 2005.

[29] J. Z. Wang, Z. H. Zheng, H. W. Li, W. T. S. Huck, and H. Sirringhaus, “Dewetting of conducting polymer inkjet droplets on patterned surfaces,” *Nat Mater*, vol. 3, no. 3, pp. 171–176, 2004.

[30] C. Priest, P. S. H. Forsberg, R. Sedev, and J. Ralston, “Structure-induced spreading of liquid in micropillar arrays,” in *Microsystem Technologies*, Feb. 2012, vol. 18, no. 2, pp. 167–173. doi: 10.1007/s00542-011-1341-8.

[31] P. S. H. Forsberg, C. Priest, M. Brinkmann, R. Sedev, and J. Ralston, “Contact line pinning on microstructured surfaces for liquids in the Wenzel state,” *Langmuir*, vol. 26, no. 2, pp. 860–865, Jan. 2010, doi: 10.1021/la902296d.

[32] J. Feng, M. T. Tuominen, and J. P. Rothstein, “Hierarchical superhydrophobic surfaces fabricated by dual-scale electron-beam-lithography with well-ordered secondary nanostructures,” *Advanced Functional Materials*, vol. 21, no. 19, pp. 3715–3722, 2011.

[33] R. D. Narhe and D. A. Beysens, “Growth dynamics of water drops on a square-pattern rough hydrophobic surface,” *Langmuir*, vol. 23, no. 12, pp. 6486–6489, 2007.

[34] Y. Liu, X. Chen, and J. H. Xin, “Can superhydrophobic surfaces repel hot water?,” *Journal of Materials Chemistry*, vol. 19, no. 31, pp. 5602–5611, 2009.

[35] A. Mahajan, W. J. Hyun, S. B. Walker, J. A. Lewis, L. F. Francis, and C. D. Frisbie, “High-resolution, high-aspect ratio conductive wires embedded in plastic substrates,” *ACS Applied Materials and Interfaces*, vol. 7, no. 3, pp. 1841–1847, Jan. 2015, doi: 10.1021/am507539a.

[36] K. C. Krogman, N. S. Zacharia, S. Schroeder, and P. T. Hammond, “Automated process for improved uniformity and versatility of layer-by-layer deposition,” *Langmuir*, vol. 23, no. 6, pp. 3137–3141, Mar. 2007, doi: 10.1021/la063085b.

[37] Y. Fang *et al.*, “A novel, facile, layer-by-layer substrate surface modification for the fabrication of all-inkjet-printed flexible electronic devices on Kapton,” *Journal of Materials Chemistry C*, vol. 4, no. 29, pp. 7052–7060, 2016, doi: 10.1039/c6tc01066k.

[38] T. Huhtamäki, X. Tian, J. T. Korhonen, and R. H. A. Ras, “Surface-wetting characterization using contact-angle measurements,” *Nat Protoc*, vol. 13, no. 7, pp. 1521–1538, 2018.

[39] K.-Y. Law, “Contact Angle Hysteresis on Smooth/Flat and Rough Surfaces. Interpretation, Mechanism, and Origin,” *Accounts of Materials Research*, 2021.

[40] T. D. Lee and A. U. Ebong, “A review of thin film solar cell technologies and challenges,” *Renewable and Sustainable Energy Reviews*, vol. 70, pp. 1286–1297, 2017.

[41] “https://www.nrel.gov/pv/assets/images/efficiency-chart.png.”

[42] “World Health Organization, 2016. Ten chemicals of major public health concern. Geneva: WHO. 2015.”.

[43] N. C. Miller and M. Bernechea, “Research Update: Bismuth based materials for photovoltaics,” *APL Materials*, vol. 6, no. 8, p. 084503, 2018.

[44] F. A. Cotton, G. Wilkinson, C. A. Murillo, M. Bochmann, and R. Grimes, *Advanced inorganic chemistry*, vol. 6. Wiley New York, 1988.

[45] A. J. Lehner *et al.*, “Electronic structure and photovoltaic application of BiI3,” *Applied Physics Letters*, vol. 107, no. 13, p. 131109, 2015.

[46] Y. Zhu *et al.*, “Vapor phase fabrication of three-dimensional arrayed BiI3 nanosheets for cost-effective solar cells,” *InfoMat*, vol. 2, no. 5, pp. 975–983, 2020.

[47] G. E. Jellison, J. O. Ramey, and L. A. Boatner, “Optical functions of BiI 3 as measured by generalized ellipsometry,” *Physical Review B*, vol. 59, no. 15, p. 9718, 1999.

[48] W.-B. Zhang, L.-J. Xiang, and H.-B. Li, “Theoretical perspective of energy harvesting properties of atomically thin BiI 3,” *Journal of Materials Chemistry A*, vol. 4, no. 48, pp. 19086–19094, 2016.

[49] U. H. Hamdeh, R. D. Nelson, B. J. Ryan, U. Bhattacharjee, J. W. Petrich, and M. G. Panthani, “Solution-processed BiI3 thin films for photovoltaic applications: Improved carrier collection via solvent annealing,” *Chemistry of Materials*, vol. 28, no. 18, pp. 6567–6574, 2016.

[50] B. W. Williamson, F. T. Eickemeyer, and H. W. Hillhouse, “Solution-Processed BiI3 Films with 1.1 eV Quasi-Fermi Level Splitting: The Role of Water, Temperature, and Solvent during Processing,” *ACS Omega*, vol. 3, no. 10, pp. 12713–12721, 2018.

[51] A. Kulkarni, T. Singh, A. K. Jena, P. Pinpithak, M. Ikegami, and T. Miyasaka, “Vapor annealing controlled crystal growth and photovoltaic performance of bismuth triiodide embedded in mesostructured configurations,” *ACS Appl Mater Interfaces*, vol. 10, no. 11, pp. 9547–9554, 2018.

[52] D. Tiwari, D. Alibhai, and D. J. Fermin, “Above 600 mV open-circuit voltage BiI3 solar cells,” *ACS Energy Letters*, vol. 3, no. 8, pp. 1882–1886, 2018.

[53] R. E. Brandt *et al.*, “Investigation of bismuth triiodide (BiI3) for photovoltaic applications,” *J Phys Chem Lett*, vol. 6, no. 21, pp. 4297–4302, 2015.

[54] B. M. Kayes, H. A. Atwater, and N. S. Lewis, “Comparison of the device physics principles of planar and radial p-n junction nanorod solar cells,” *J Appl Phys*, vol. 97, no. 11, p. 114302, 2005.

[55] Z. Fan *et al.*, “Three-dimensional nanopillar-array photovoltaics on low-cost and flexible substrates,” *Nat Mater*, vol. 8, no. 8, pp. 648–653, 2009.

[56] M. Yu, Y.-Z. Long, B. Sun, and Z. Fan, “Recent advances in solar cells based on one-dimensional nanostructure arrays,” *Nanoscale*, vol. 4, no. 9, pp. 2783–2796, 2012.

[57] P. M. Rao, I. S. Cho, and X. Zheng, “Flame synthesis of WO3 nanotubes and nanowires for efficient photoelectrochemical water-splitting,” *Proceedings of the Combustion Institute*, vol. 34, no. 2, pp. 2187–2195, 2013.

[58] G. M. Pound, M. T. Simnad, and L. Yang, “Heterogeneous nucleation of crystals from vapor,” *J Chem Phys*, vol. 22, no. 7, pp. 1215–1219, 1954.

[59] F. Dinelli, M. Murgia, P. Levy, M. Cavallini, F. Biscarini, and D. M. de Leeuw, “Spatially correlated charge transport in organic thin film transistors,” *Physical Review Letters*, vol. 92, no. 11, p. 116802, 2004.